

# Hyperbolic Universes with a Horned Topology and the CMB Anisotropy

Ralf Aurich<sup>1</sup>, Sven Lustig<sup>1</sup>, Frank Steiner<sup>1</sup> and Holger Then<sup>2</sup>

<sup>1</sup>Abteilung Theoretische Physik, Universität Ulm,  
Albert-Einstein-Allee 11, D-89069 Ulm, Germany

<sup>2</sup>School of Mathematics, University of Bristol,  
University Walk, Bristol, BS8 1TW, United Kingdom

**Abstract.** We analyse the anisotropy of the cosmic microwave background (CMB) in hyperbolic universes possessing a non-trivial topology with a fundamental cell having an infinitely long horn. The aim of this paper is twofold. On the one hand, we show that the horned topology does not lead to a flat spot in the CMB sky maps in the direction of the horn as stated in the literature. On the other, we demonstrate that a horned topology having a finite volume could explain the suppression of the lower multipoles in the CMB anisotropy as observed by COBE and WMAP.

PACS numbers: 98.80.-k, 98.70.Vc, 98.80.Es

## 1. Introduction

A fundamental problem in cosmology is the large-scale geometry of the Universe, in particular its spatial curvature and topology. Since the Einstein gravitational field equations are differential equations, they determine the local properties of space-time, but not the global structure of the Universe at large. In the so-called concordance model of cosmology it is assumed that the Universe is at large scales spatially flat and possesses the trivial topology, implying that it has infinite volume. In the framework of inflationary scenarios, these properties are supposed to be determined by the initial conditions at the Big Bang. However, since we are lacking a theory of quantum gravity, the initial conditions cannot be derived from first principles. Instead, one can analyse the recent astronomical data, in particular on the cosmic microwave background (CMB) radiation, in order to deduce the curvature and the topology of the Universe at large scales.

In 1992, COBE [1] made the spectacular discovery of the temperature fluctuations of the CMB and thus provided important clues about the early Universe and its time evolution. Expanding the observed temperature fluctuations  $\delta T(\hat{n})$  across the microwave sky into spherical harmonics  $Y_l^m(\hat{n})$ , yields the expansion coefficients  $a_{lm}$  which in turn

lead to the *multipole moments*

$$C_l := \frac{1}{2l+1} \sum_{m=-l}^l |a_{lm}|^2 \quad (1)$$

and the *angular power spectrum*  $\delta T_l^2 := l(l+1)C_l/(2\pi)$ . In particular, COBE [1] detected in the angular power spectrum of the CMB a low quadrupole moment  $C_2$  corresponding to a strange suppression of power on large angular scales. It was soon realized that although the standard cosmological models are in agreement with the CMB anisotropy on small and medium scales, they fail to match the loss of power on large angular scales, especially those corresponding to the quadrupole moment. This observation was one of the motivations to study non-trivial topologies (see the reviews [2, 3]). In particular, compact hyperbolic universes were studied by several authors [4, 5, 6, 7, 8, 9, 10, 11]. For these compact hyperbolic universes, it was shown that the non-trivial topology leads indeed to a suppression of  $C_l$  for small values of  $l$ . Thus the observed loss of power on large angular scales was interpreted as a clear hint to a non-trivial topology of our Universe.

The first findings of NASA's explorer mission "Wilkinson Microwave Anisotropy Probe" (WMAP) [12] have tremendously increased our knowledge of the temperature fluctuations of the CMB, since WMAP has measured the anisotropy of the CMB radiation over the full sky with high accuracy. The WMAP data confirm not only COBE's measurement of the low quadrupole moment  $C_2$ , but display in the temperature (auto-) correlation function  $C(\vartheta)$  ( $\hat{n} \cdot \hat{n}' = \cos \vartheta$ )

$$C(\vartheta) \simeq \frac{1}{4\pi} \sum_{l=2}^{\infty} (2l+1) C_l P_l(\cos \vartheta) \quad (2)$$

very weak correlations at wide angles,  $70^\circ \lesssim \vartheta \lesssim 150^\circ$ , see the dashed curve in figure 1. (Note that the monopole and dipole are not included in the sum (2).) At the largest angles,  $\vartheta \gtrsim 160^\circ$ , the WMAP-data display even a "correlation hole", i. e. negative values of  $C(\vartheta)$ . In figure 1 we also show as a dotted curve the theoretical prediction according to the concordance model using the best-fit values for the cosmological parameters as obtained by WMAP [12]. It is seen that the concordance model, i. e. the best-fit  $\Lambda$ CDM model, does not reproduce the experimentally observed suppression at  $\vartheta \gtrsim 60^\circ$  and the observed correlation hole.

Since the correlation function  $C(\vartheta)$  emphasizes large angular scales and thus the low  $l$ -range, it is an ideal indicator function to search for a fingerprint of a possible non-trivial topology of the Universe.

The evidence for a low quadrupole and missing power on large scales is, however, currently heavily discussed. The low value of the quadrupole obtained by the WMAP team [12] has been criticized by the way how the foregrounds [13] are taken into account which are mainly caused by free-free, synchrotron and dust emission. Alternative reconstructions of the true cosmological signal from the five frequency bands measured by WMAP are discussed in [14, 15] which lead to a higher quadrupole moment. The

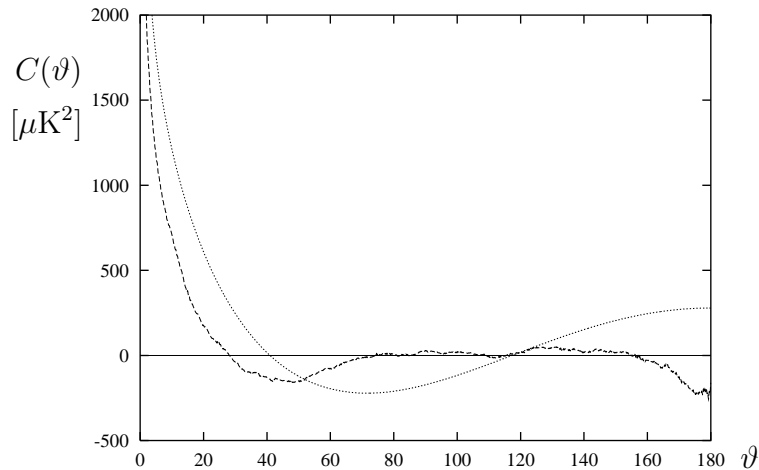


**Figure 1.** The correlation function  $C(\vartheta)$  from the WMAP-data (dashed curve) in comparison with the concordance model (dotted curve).

observation that the plane of the quadrupole and two of the three planes of the octopoles are aligned towards the ecliptic might be seen as a hint of an unknown source or sink of CMB radiation in the outer solar system or as an unrecognized systematic [16]. The influence of the approximation of the likelihood function used for the angular power spectra analysis is investigated in [17], where for the lowest multipoles an exact likelihood function estimation is presented. The statistical significance of the low value of the quadrupole moment is also discussed in [18] who found the WMAP results to be consistent with the concordance  $\Lambda$ CDM model. The statistic is limited by the one-sky realization we are able to measure, also called cosmic variance. To circumvent this problem it is suggested to utilize the fact that the CMB polarization is sourced by the local temperature quadrupole. On the one hand, the polarization signal contains information about the quadrupole moment at the reionization epoch. This could lead to a probability for the observed quadrupole moment of the order of  $10^{-4}$  [19] compared with the concordance model. On the other hand, future measurements of the linear polarization of the CMB towards clusters of galaxies can betray the local quadrupole moment at the location of the cluster [20, 21, 22] thus circumventing the cosmic variance limit.

Furthermore, we would like to mention that “the question whether the geometry of the three-dimensional space of astronomy might be non-Euclidean” [23] has already been posed by Schwarzschild [24, 25, 26] in 1900, fifteen years before the founding of general relativity! He stated the problem as follows (see p.32 in [24]): “As must be known to you, during this century [meaning the 19th century] one has developed non-Euclidean geometry (besides Euclidean geometry), the chief examples of which are the so-called spherical and pseudo-spherical spaces. We can wonder how the world would appear in a spherical or pseudo-spherical geometry with possibly a finite radius of curvature ... One would then find oneself, if one will, in a geometrical fairyland; and one does not know whether the beauty of this fairyland may in fact be realized

in nature.” Schwarzschild “actually estimated limits to the radius of curvature of the three-dimensional space with the astronomical data available at his time and concluded that if the space is hyperbolic its radius of curvature cannot be less than 64 light years and that if the space is spherical its radius of curvature must at least be 1600 light years” [23]. In an Addendum to his article “On the permissible scale of curvature of space” [25] he mentioned also the possibility of spaces with non-trivial topology by referring to Clifford-Klein space forms. And he emphasized that such spaces do not necessarily lead to infinite universes as commonly assumed, even in the case of Euclidean or hyperbolic geometry. Schwarzschild concluded that the only condition imposed by astronomical data is that the volume of the Universe must be larger than the visible system of stars.

It is the purpose of this paper to investigate two models of the Universe whose global topology is not the universal covering space of their spatial geometry. The spatial geometry of the models is the pseudo-spherical or hyperbolic space, i. e. it has negative curvature. The corresponding hyperbolic universes are non-compact and possess an infinitely long horn. The first model was introduced in 1976 by Sokolov and Starobinskii [27] and is described by a fundamental cell  $\mathcal{F}$  having infinite volume. The second model, called the Picard model [28], has also an infinitely long horn, but nevertheless possesses a finite volume. The Picard model has been investigated in detail in the context of quantum chaos [29, 30, 31].

The Sokolov-Starobinskii model has been studied already in [27] and [32] (see also the review [3]). In [32] it has been claimed that the periodic horn topology produces a flat spot in the temperature map of the CMB even when multiple images of astronomical sources are unobservable. The flat spot, i. e. a large flat region in the CMB sky map corresponding to a negligibly small metric perturbation, is argued in [32] to result from the exponential decay of the eigenmodes in the direction of the horn.

We shall show in the following that the flat spot found in [32] is a consequence of a too low wavenumber cut-off  $k_c$ . For the cut-off chosen in [32], the eigenmodes cannot produce indeed a perturbation in the horn at the position which corresponds to the distance of the surface of last scattering (SLS). As a consequence, the sky maps computed in [32] do not show temperature fluctuations in the horn. However, if the cut-off is sufficiently increased, we shall demonstrate that there is no suppression in the horn and therefore no flat spot.

The universes described by the Sokolov-Starobinskii and Picard model, respectively, possess negative spatial curvature in contrast to the concordance model corresponding to a spatially flat universe. Therefore the question arises whether a negatively curved universe is realized in nature. In [33, 34] we have analysed the CMB data and the magnitude redshift relation of supernovae type Ia in the framework of quintessence models and have shown that these data are consistent with a nearly flat hyperbolic geometry of our Universe if the optical depth  $\tau$  to the SLS is not too big. The restriction comes from the large amplitude of the fluctuations at large scales in the CMB. However, it was shown in [35] that by replacing the quintessence component having a rest frame sound velocity of  $c_s = c$  by a generalized dark matter component [36] with a vanishing

rest frame sound velocity  $c_s = 0$ , the amplitude in the CMB anisotropy is much smaller at large scales. Thus with such a generalized dark matter component universes with negative curvature are permissible even for larger optical depths  $\tau$ .

Recently, an ellipticity analysis of the CMB maps has been reported [37, 38, 39] which gives further support to a hyperbolic spatial geometry of the Universe. In these analyses hot and cold anisotropy spots in the CMB maps have been studied in terms of shape for various temperature thresholds. Analysing with the same algorithm the COBE-DMR, BOOMERanG 150 GHz and WMAP maps, an ellipticity of the anisotropy spots has been found of the same average value (around 2) for these experiments. The WMAP data confirm the effect for scales both smaller and larger than the horizon at the SLS. This suggests that the effect is not due to physical effects at the SLS, and can arise after, while the photons are moving freely in the Universe.

Finally, we would like to mention that recently a model was presented [40] possessing positive curvature and a finite volume with the shape of the Poincaré dodecahedral space. The authors of ref. [40] calculated the CMB multipoles for  $l = 2, 3$  and 4, set the overall normalization factor to match the WMAP data at  $l = 4$  and examined the prediction for  $l = 2$  and 3. They found a weak suppression of the power at  $l = 3$  and strong suppression at  $l = 2$  in agreement with the WMAP observations. However, in ref. [40] only the modes up to  $k_c = 30$  have been used, and it thus remains the question about how this low cut-off affects the integrated Sachs-Wolfe (ISW) contribution. Our experience shows that increasing the cut-off usually enhances the ISW contribution.

## 2. The CMB anisotropy

The CMB anisotropy is computed for universes whose background models are described by the Friedmann equation ( $c = 1$ )

$$H^2 := \left(\frac{a'}{a^2}\right)^2 = \frac{8\pi G}{3}\varepsilon_{\text{tot}} - \frac{K}{a^2} \quad , \quad K \in \{-1, 0, +1\} \quad . \quad (3)$$

Here  $a = a(\eta)$  denotes the cosmic scale factor as a function of conformal time  $\eta = \int \frac{dt}{a}$  and  $K$  the spatial curvature. The total energy density  $\varepsilon_{\text{tot}}$  is given by a sum of 4 components: radiation, baryonic matter, cold dark matter and a positive cosmological constant  $\Lambda$ . In this paper, we consider only scalar perturbations, i. e. vector and tensor modes are neglected. Furthermore, we are mainly interested in fluctuations on scales larger than the size of the horizon at the time of recombination since these fluctuations should contain the fingerprint of a non-trivial topology. Above the size of the horizon the temperature anisotropy can be computed neglecting physical processes important only on small scales such as the Silk damping. The metric with scalar perturbations is written in the conformal-Newtonian gauge in terms of scalar functions  $\Phi$  and  $\Psi$  as

$$ds^2 = a^2(\eta) \left\{ (1 + 2\Phi)d\eta^2 - (1 - 2\Psi)\gamma_{ij}dx^i dx^j \right\} \quad ,$$

where  $\Phi = \Psi$  for an energy-momentum tensor  $T_{\mu\nu}$  with  $T_{ij} = 0$  for  $i \neq j$  and  $i, j = 1, 2, 3$ . ( $\gamma_{ij}$  denotes the metric of the 3-space.) The metric perturbation  $\Phi$  is

expanded into the eigenfunctions  $\psi_k(\vec{x})$  of the (negative) Laplace-Beltrami operator  $\Delta$ , i. e.  $(\Delta + E)\psi_k(\vec{x}) = 0$  with  $k = \sqrt{E + K}$ , e. g. for a discrete spectrum

$$\Phi(\eta, \vec{x}) = \sum_{n=1}^{\infty} \Phi_{k_n}(\eta) \psi_{k_n}(\vec{x}) \quad . \quad (4)$$

In the *single fluid approximation*, the radiation, the baryonic matter and the cold dark matter are treated as one fluid which is valid on scales larger than the horizon size at recombination. There the entropy perturbation  $\delta S$  is thus negligible, i. e.  $\delta S = 0$ . Then the evolution of the metric perturbation  $\Phi(\eta, \vec{x})$  gives in first-order perturbation theory in the conformal-Newtonian gauge [41]

$$\Phi'' + 3\hat{H}(1 + c_s^2)\Phi' - c_s^2\Delta\Phi + \{2\hat{H}' + (1 + 3c_s^2)(\hat{H}^2 - K)\}\Phi = 0 \quad , \quad (5)$$

where  $\hat{H} := a'/a$ . The quantity  $c_s^2 = (3 + \frac{9}{4}\varepsilon_{\text{mat}}/\varepsilon_r)^{-1}$  can be interpreted as the sound velocity. Specifying the initial perturbation  $\Phi$  at  $\eta = 0$  such that it corresponds to a scale-invariant Harrison-Zel'dovich spectrum (see [11];  $\hat{\eta} = 2\sqrt{\Omega_r\Omega_{\text{curv}}}/\Omega_{\text{mat}}$ )

$$\Phi_{\vec{k}}(0) = \frac{\alpha}{\sqrt{k(k^2 - K)}} \quad \text{and} \quad \Phi'_{\vec{k}}(0) = -\frac{\Phi_{\vec{k}}(0)}{8\hat{\eta}} \quad , \quad (6)$$

where  $\Phi_{\vec{k}}(\eta)$  denote the expansion coefficients of  $\Phi(\eta, \vec{x})$  (see equations (12) and (14) below), allows the computation of the time-evolution of the metric perturbation  $\Phi$ . Here we have defined the density parameters  $\Omega_x := \varepsilon_x(\eta_0)/\varepsilon_{\text{crit}}$  with  $\varepsilon_{\text{crit}} = 3H_0^2/(8\pi G)$  for  $x = r$  (=radiation), mat (= baryonic + cold dark matter (CDM)), and curv (= curvature) with  $\Omega_{\text{curv}} = 1 - \Omega_{\text{tot}}$ . The Hubble constant  $H_0 = h \times 100 \text{ km s}^{-1}\text{Mpc}^{-1}$  is set in the following to  $h = 0.65$ . ( $\alpha$  is a normalization constant and  $\eta_0$  denotes the conformal time at the present epoch.) The metric perturbation  $\Phi$  in turn gives the input to the Sachs-Wolfe formula [42] which reads for isentropic initial conditions

$$\frac{\delta T}{T}(\hat{n}) = 2\Phi(\eta_{\text{SLS}}, \vec{x}(\eta_{\text{SLS}})) - \frac{3}{2}\Phi(0, \vec{x}(0)) + 2 \int_{\eta_{\text{SLS}}}^{\eta_0} d\eta \frac{\partial\Phi(\eta, \vec{x}(\eta))}{\partial\eta} \quad , \quad (7)$$

from which one obtains the desired temperature fluctuations  $\delta T$  of the CMB. Here  $\hat{n}$  denotes the unit vector in the direction of  $\vec{x}(\eta_{\text{SLS}}) - \vec{x}(\eta_0)$ , i. e. in the direction from which the photons arrive. The single fluid approximation has been used in a lot of earlier papers concerning the CMB anisotropy for non-trivial topologies. We summarized this approach here, because we need it for the comparison with earlier papers.

We use in our computations the *tight-coupling approximation* in which only the radiation and the baryonic matter is approximated as a single fluid before recombination, whereas the cold dark matter component is independent. The following summary of the tight-coupling approximation follows the lines of Mukhanov [43]. The Sachs-Wolfe formula reads for the tight-coupling approximation

$$\begin{aligned} \frac{\delta T}{T}(\hat{n}) = & \int d^3k \left[ \left( \Phi_{\vec{k}}(\eta) + \frac{\delta_{\vec{k},r}(\eta)}{4} + \frac{a(\eta)V_{\vec{k},r}(\eta)}{E_{\vec{k}}} \frac{\partial}{\partial\tau} \right) \psi_{\vec{k}}(\tau(\eta), \theta, \phi) \right]_{\eta=\eta_{\text{SLS}}} \\ & + 2 \int d^3k \int_{\eta_{\text{SLS}}}^{\eta_0} d\eta \frac{\partial\Phi_{\vec{k}}(\eta)}{\partial\eta} \psi_{\vec{k}}(\tau(\eta), \theta, \phi) \quad , \quad (8) \end{aligned}$$

where the  $\vec{k}$ -integration has to be interpreted as a summation in the case of a discrete spectrum.  $(\tau(\eta), \theta, \phi)$  denote the spherical coordinates of the photon path in the direction  $\hat{n}$ . Here,  $\delta_{\vec{k},r}(\eta)$  is the expansion coefficient of the relative perturbation in the radiation component, and  $V_{\vec{k},r}(\eta)$  is the expansion coefficient of the spatial covariant divergence of the velocity field of the tightly coupled radiation-baryon components. The term in equation (8) which has to be evaluated at  $\eta = \eta_{\text{SLS}}$  is computed using the tight-coupling approximation. The second term, i.e. the integrated Sachs-Wolfe effect, is computed with a decoupled baryon component. In the case of isentropic initial conditions, the relation between the perturbation in the radiation and baryonic component during the tight-coupling phase is  $\delta_{\vec{k},b} = \frac{3}{4}\delta_{\vec{k},r}$ . The time-evolution of the perturbations is determined by the following system of differential equations which has to be solved numerically. For the metric perturbation, one obtains ( $E_{\vec{k}} = k^2 - K$ )

$$\frac{d}{d\eta}\Phi_{\vec{k}}(\eta) + \frac{a(\eta)}{a'(\eta)}\left(\frac{1}{3}E_{\vec{k}} + \left(\frac{a'(\eta)}{a(\eta)}\right)^2 - K\right)\Phi_{\vec{k}}(\eta) = -\frac{4\pi G}{3}\frac{a^3(\eta)}{a'(\eta)}\delta\varepsilon_{\vec{k}}(\eta) \quad ,$$

where the energy perturbation  $\delta\varepsilon_{\vec{k}}(\eta)$  before recombination is given by

$$\delta\varepsilon_{\vec{k}}(\eta) = \epsilon_{\text{CDM}}(\eta)\delta_{\vec{k},\text{CDM}}(\eta) + \frac{\epsilon_r(\eta)}{3c_s^2}\delta_{\vec{k},r}(\eta) \quad ,$$

with  $c_s^2 = (3 + \frac{9}{4}\varepsilon_b/\varepsilon_r)^{-1}$ , and after recombination by

$$\delta\varepsilon_{\vec{k}}(\eta) = \epsilon_{\text{CDM}}(\eta)\delta_{\vec{k},\text{CDM}}(\eta) + \epsilon_b(\eta)\delta_{\vec{k},b}(\eta) + \epsilon_r(\eta)\delta_{\vec{k},r}(\eta) \quad .$$

The energy and momentum conservation equations for the CDM component read

$$\frac{d}{d\eta}\left(\delta_{\vec{k},\text{CDM}}(\eta) - 3\Phi_{\vec{k}}(\eta)\right) = -a(\eta)V_{\vec{k},\text{CDM}}(\eta)$$

and

$$\frac{d}{d\eta}\left(a^2(\eta)V_{\vec{k},\text{CDM}}(\eta)\right) = a(\eta)E_{\vec{k}}\Phi_{\vec{k}}(\eta) \quad ,$$

respectively. For the radiation component, the energy conservation equation is

$$\frac{d}{d\eta}\left(\delta_{\vec{k},r}(\eta) - 4\Phi_{\vec{k}}(\eta)\right) = -\frac{4}{3}a(\eta)V_{\vec{k},r}(\eta) \quad ,$$

whereas the momentum conservation equation is before recombination given by

$$\frac{d}{d\eta}\left(\frac{1}{c_s^2}a(\eta)V_{\vec{k},r}(\eta)\right) = E_{\vec{k}}\left(\frac{1}{c_s^2}\Phi_{\vec{k}}(\eta) + \frac{3}{4}\delta_{\vec{k},r}(\eta)\right)$$

and after recombination by

$$\frac{d}{d\eta}\left(a(\eta)V_{\vec{k},r}(\eta)\right) = E_{\vec{k}}\left(\Phi_{\vec{k}}(\eta) + \frac{1}{4}\delta_{\vec{k},r}(\eta)\right) \quad .$$

After recombination the energy and momentum conservation equations for the baryonic component are analogous to that of the CDM component. The initial conditions of the various components depend all on that of  $\Phi_{\vec{k}}(0)$  as

$$\delta_{\vec{k},r}^-(0) = \frac{4}{3} \delta_{\vec{k},b}^-(0) = \frac{4}{3} \delta_{\vec{k},\text{CDM}}^-(0) = -2 \Phi_{\vec{k}}^-(0)$$

and

$$V_{\vec{k},r}^-(0) = V_{\vec{k},b}^-(0) = V_{\vec{k},\text{CDM}}^-(0) = E_{\vec{k}} \frac{H_0 |\Omega_{\text{curv}}|}{2\sqrt{\Omega_r}} \Phi_{\vec{k}}^-(0) \quad .$$

The initial power spectrum  $\Phi_{\vec{k}}(0)$  is taken as the usual Harrison-Zel'dovich spectrum having a spectral index  $n_s = 1$  which is in agreement with the current observations [44, 45]. Furthermore, we do not take a running spectral index into account since, as shown in [45], only the first three multipoles  $C_2$ ,  $C_3$  and  $C_4$  are responsible for a non-vanishing running spectral index, and it is just these multipoles which are most strongly modified by a fundamental cell of finite volume.

### 3. The Sokolov-Starobinskii model

The model was introduced by Sokolov and Starobinskii [27] for cosmological studies. In order to describe the model, we have to introduce the hyperbolic three-space for which a wealth of models exists, see e. g. [46]. Here we choose the upper half-space model

$$\mathfrak{H}_3 = \{(x_1, x_2, x_3) \in \mathbb{R}^3 \mid x_3 > 0\} \quad , \quad (9)$$

equipped with the Riemannian metric

$$ds^2 = \frac{dx_1^2 + dx_2^2 + dx_3^2}{x_3^2} \quad (10)$$

corresponding to a constant Gaussian curvature  $K = -1$ . The geodesics of a particle moving freely in the upper half-space are straight lines and semicircles perpendicular to the  $x_1$ - $x_2$ -plane.

In the Sokolov-Starobinskii model [27] one identifies points periodically along  $x_1$  and  $x_2$  according to  $(x_1, x_2, x_3) \equiv (x_1 + \mu a, x_2 + \nu b, x_3)$  with  $\mu, \nu \in \mathbb{Z}$ . The positive constants  $a$  and  $b$  define the toroidal topology. The Sokolov-Starobinskii model has an infinitely long horn in the positive  $x_3$  direction whose physical cross section decreases according to (10) with increasing  $x_3$ . On the other hand, towards  $x_3 \rightarrow 0^+$  the cross section increases without bound. Thus the fundamental cell  $\mathcal{F} = \{\vec{x} \in \mathbb{R}^3 \mid 0 \leq x_1 < a, 0 \leq x_2 < b, x_3 > 0\}$  has infinite volume.

The eigenmodes of the Laplace-Beltrami operator on  $\mathfrak{H}_3$

$$\Delta = x_3^2 \left( \frac{\partial^2}{\partial x_1^2} + \frac{\partial^2}{\partial x_2^2} + \frac{\partial^2}{\partial x_3^2} \right) - x_3 \frac{\partial}{\partial x_3}$$

consist of decaying modes and plane waves. The decaying modes are given by ( $k > 0$ ,  $(m, n) \in (\mathbb{N}_0 \times \mathbb{N}_0) - \{0, 0\}$ )

$$\psi_{kmn}(\vec{x}) = N_{kmn} x_3 K_{ik}(Qx_3) \begin{pmatrix} \sin \frac{2\pi m}{a} x_1 \\ \cos \frac{2\pi m}{a} x_1 \end{pmatrix} \begin{pmatrix} \sin \frac{2\pi n}{b} x_2 \\ \cos \frac{2\pi n}{b} x_2 \end{pmatrix} \quad , \quad (11)$$



with

$$N_{kmn} = \sqrt{\frac{2k \sinh \pi k}{\pi^2} \cdot \frac{(2 - \delta_{m0})(2 - \delta_{n0})}{ab}} \quad \text{and} \quad Q = 2\pi \sqrt{\left(\frac{m}{a}\right)^2 + \left(\frac{n}{b}\right)^2} > 0 .$$

Here  $K_{ik}(z)$  denotes the modified Bessel function of order  $ik$ . Due to the above normalization factor  $N_{kmn}$ , the eigenmodes (11) are normalized as follows

$$\int_{\mathcal{F}} d\mu \psi_{kmn}(\vec{x}) \psi_{k'm'n'}(\vec{x}) = \delta(k - k') \delta_{m,m'} \delta_{n,n'} \quad \text{with} \quad d\mu = \frac{dx_1 dx_2 dx_3}{x_3^3} .$$

Three examples of the eigenmodes (11) for  $k = 20$  and three different pairs of  $m$  and  $n$  are shown in figure 2. The domain, where the modes dominate, decreases in  $x_3$  with increasing  $Q$ .

The metric perturbation corresponding to these modes can then be expanded as

$$\Phi(\eta, \vec{x}) = \int_0^\infty dk \Phi_k(\eta) \sum'_{m,n} r(k, m, n) \psi_{kmn}(\vec{x}) , \quad (12)$$

where the prime at the sum indicates that the term with  $m = n = 0$  is excluded. The  $r(k, m, n)$  are real Gaussian expansion coefficients with mean value zero and variance independent of  $k$  such that the amplitude  $\Phi_k(\eta)$  describes the usual power spectrum (6). This leads to the usual statistical properties of the fluctuations far away from the horn. The coefficients  $r(k, m, n)$  do not carry any information about the direction of the horn. The information about the horn is only contained in the eigenmodes of the Laplacian.

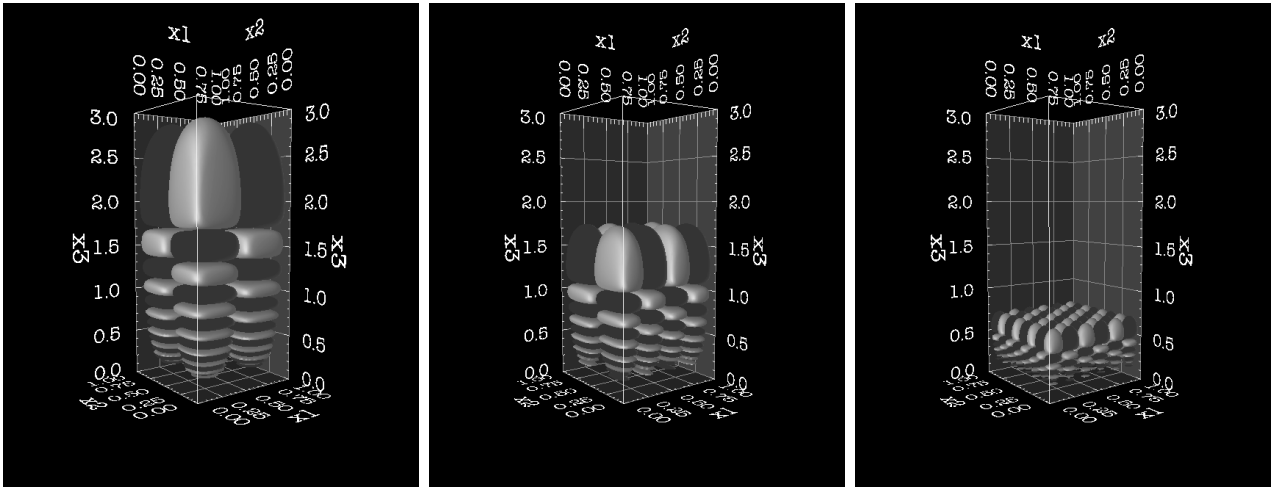


**Figure 2.** Three eigenmodes (11) using two sines for the eigenvalue  $k = 20$  and  $a = b = 1$  are shown. The eigenmodes belong to  $(m, n) = (1, 1)$ ,  $(m, n) = (2, 1)$  and  $(m, n) = (3, 4)$ , respectively, from left to right. With increasing values of  $Q$ , the exponential suppression of the  $K$ -Bessel function occurs earlier in the horn. The suppression towards  $x_3 \rightarrow 0$  is due to the  $x_3$ -factor in eq. (11).

The eigenmodes (11) decay exponentially in the horn due to the  $K$ -Bessel function. In addition to (11) there are further eigenmodes which constitute non-decaying plane

wave solutions in the horn. They are given by ( $k > 0$ )

$$\psi_k^{\text{s,c}}(\vec{x}) = \frac{1}{\sqrt{\pi ab}} x_3 \begin{pmatrix} \sin(k \ln x_3) \\ \cos(k \ln x_3) \end{pmatrix} . \quad (13)$$

These plane wave solutions are normalized similar to (11) as

$$\int_{\mathcal{F}} d\mu \psi_k^{\text{s,c}}(\vec{x}) \psi_{k'}^{\text{s,c}}(\vec{x}) = \delta(k - k') .$$

The metric perturbation can be expanded analogously to (12), but without the  $m$  and  $n$  summation

$$\Phi^{\text{s,c}}(\eta, \vec{x}) = \int_0^\infty dk r(k) \Phi_k(\eta) \psi_k^{\text{s,c}}(\vec{x}) , \quad (14)$$

where  $r(k)$  are real Gaussian expansion coefficients.

These solutions were not taken into account in the computation of the density perturbations in [27, 32]. In [27] it was argued that they should be omitted since they are not bounded as  $x_3 \rightarrow \infty$ . Constructing small perturbations from (13) would then require a fine-tuned superposition of these solutions, which would contradict the statistical hypothesis.

Here, a remark is in order concerning the numerical evaluation of the  $k$ -integrals (12) and (14) in the case that the integrands contain a Gaussian random function  $r(k, m, n)$  or  $r(k)$ . In the case of a discrete  $k$ -spectrum there is no problem. The integral is then replaced by a sum, as in equation (4), and each mode  $k_n$  occurring in the spectrum comes with an independent Gaussian random variable. But in the case of a continuous  $k$ -spectrum there arises the question of how small the step size has to be in order to approximate the integral numerically. Since the integrand is erratic, one cannot rely on the usual arguments concerning an approximation as, say, a Riemannian sum. Even infinitesimally close values of  $k$  possess uncorrelated coefficients due to the Dirac-delta  $\delta(k - k')$  in the correlation function  $\langle r(k)r(k') \rangle$ . E.g. consider a unit interval  $\Delta k = 1$  and approximate the integral on  $\Delta k$  by  $N$  terms. It is clear that in the limit  $N \rightarrow \infty$  the approximation to the integral approaches zero due to the increasing number of cancellations among the random terms. This implies that the normalization factor  $\alpha$  which is used to normalize the fluctuation to the amplitude of COBE or WMAP depends on the discretization used in the approximation of the integrals. The value of  $N$  has at least to be so large that there are many evaluation points on an interval where the integrand without the Gaussian random variable is nearly constant. Consider the mode  $\psi_k^{\text{s}}(\vec{x})$ , eq. (13), having the simple  $x_3$ -dependence  $x_3 \sin(k \ln x_3)$ . This implies that in order to simulate a Gaussian random field there is for a fixed  $N$  a maximal value of  $x_3$  such that there are enough evaluation points for each sine-oscillation. Thus one has to ensure that there are no parts of the SLS so high in the horn, i.e. have corresponding high values of  $x_3$ , that the CMB simulation is not valid for the chosen value of  $N$ . We use in the following simulations a Gaussian quadrature with 16 evaluation points on the unit interval  $\Delta k = 1$ . This is sufficient for the chosen cosmological parameters. Finally,

let us remark that, if there are several contributing integrals, their normalization factors can be different if their integrands without the random variable oscillate on different spatial scales.

As a first application let us consider only the decaying modes (11) as it is done in [27, 32]. In [32] the temperature fluctuations  $\delta T/T$  are computed for the Sokolov-Starobinskii model and it is claimed that the periodic horn topology produces a flat spot in the sky map of the cosmic microwave radiation. The flat spot, i. e. a negligible perturbation in the horn, is claimed to be the result of the asymptotic behaviour of the eigenmodes (11) which are exponentially declining for  $z = Qx_3 \gtrsim k$ , because of  $K_{ik}(z) \simeq \sqrt{\frac{\pi}{2z}}e^{-z}$  in this range. Modes with  $k \lesssim 2\pi x_3$  give a negligible contribution at  $x_3$  where the smallest possible value for  $Q$ , i. e.  $Q = 2\pi$  in the case  $a = b = 1$ , is considered, since these are the modes which reach as far as possible into the horn. In [32] the cut-off in  $k$  is so low that the modes cannot produce a perturbation in the horn at the position which corresponds to the distance of the surface of last scattering. As a consequence, the sky maps computed in [32] do not show temperature fluctuations in the horn. Increasing, however, the cut-off from the low value  $k_c = 10$  used in [32] to the value  $k_c = 140$  shows that there are indeed fluctuations in the horn as it will be demonstrated below.

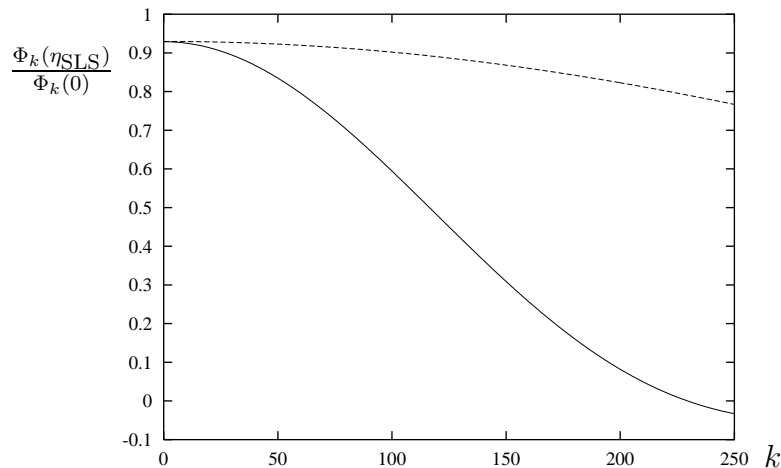


**Figure 3.** The  $k$ -dependence of  $\Phi_k(\eta_{\text{SLS}})/\Phi_k(0)$  in the single-fluid approximation is shown for a model including radiation with  $\Omega_{\text{mat}} = 0.3$  and  $\Omega_{\Lambda} = 0$  (full curve) and a nearly flat one with  $\Omega_{\text{mat}} = 0.3$  and  $\Omega_{\Lambda} = 0.65$  (dashed curve).

There is nevertheless a subtle effect which can still suppress the amplitude of the perturbations in the horn even in the case of a high cut-off  $k_c$ . As the above discussion has emphasized, it is important to include modes with sufficiently high values of  $k$ . If, however, the time evolution of  $\Phi_k(\eta)$  leads to a too strong suppression of these modes at the surface of last scattering, i. e. if  $\Phi_k(\eta_{\text{SLS}})$  declines as a function of  $k$  too fast at the values of  $k$  which generate anisotropy in the horn, then these modes cannot contribute as much as they would for a nearly  $k$ -independent  $\Phi_k(\eta_{\text{SLS}})$ . A pure matter model is

considered in [32] for which the time evolution of  $\Phi_k(\eta)/\Phi_k(0)$  is independent of  $k$

$$\Phi_k^{\text{mat}}(\eta) = \Phi_k^{\text{mat}}(0) \frac{5(\sinh^2 \eta - 3\eta \sinh \eta + 4 \cosh \eta - 4)}{(\cosh \eta - 1)^3} . \quad (15)$$

Therefore this effect does not occur in the calculation in [32]. In general, however, especially if one takes also radiation into account, equation (5) leads to a  $k$ -dependent time evolution of  $\Phi_k(\eta)/\Phi_k(0)$  as can be seen in figure 3 where  $\Phi_k(\eta_{\text{SLS}})/\Phi_k(0)$  is shown for two models containing also radiation, one with  $\Omega_{\text{mat}} = 0.3$  and  $\Omega_{\Lambda} = 0$ , and a nearly flat one with  $\Omega_{\text{mat}} = 0.3$  and  $\Omega_{\Lambda} = 0.65$ . The model with  $\Omega_{\text{tot}} = 0.3$  has a much stronger  $k$ -dependence as the nearly flat model. Notice that for a pure matter model one has  $\Phi_k(\eta_{\text{SLS}})/\Phi_k(0) = \text{const.}$  The value of  $\Phi_k(\eta)$  at  $\eta_{\text{SLS}}$  plays an important role because it describes the metric perturbation at recombination and via eq. (7) the CMB anisotropy.

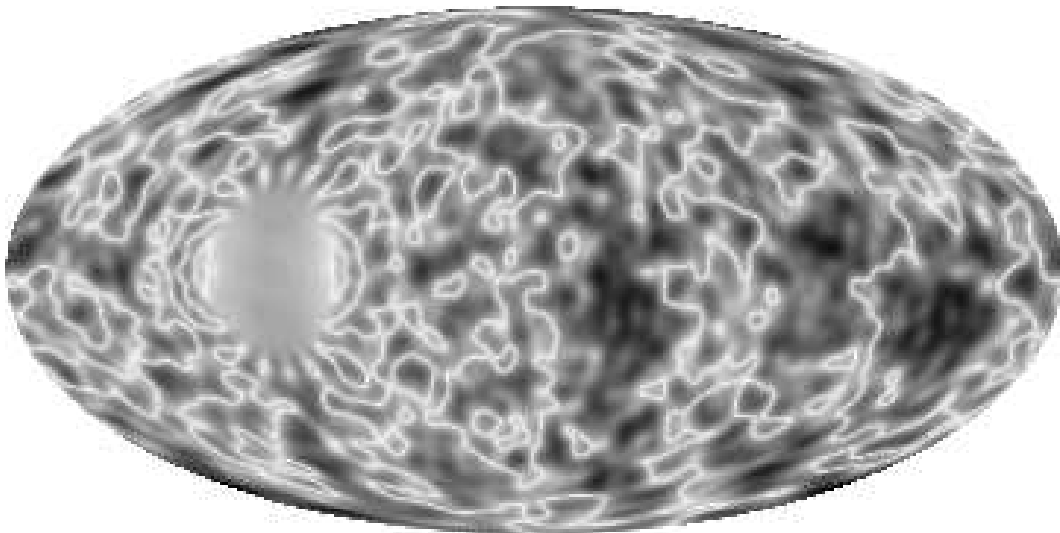


**Figure 4.** The CMB anisotropy  $\delta T$  for the Sokolov-Starobinskii model for  $\Omega_{\text{mat}} = 0.3$  and  $\Omega_{\Lambda} = 0$  with a cut-off  $k_c = 10$  using a Gaussian superposition of the modes (11). The white “curves” belong to  $\delta T = 0$  whereas increasing darkness corresponds to increasing deviations from  $\delta T = 0$ .

Let us now discuss the cosmic microwave anisotropy of the Sokolov-Starobinskii model, which is here computed using the tight-coupling approximation. In contrast to [32], we are not using a pure matter model and include the naive and integrated Sachs-Wolfe effect as well as the Doppler effect. The observer is located at  $(x_1, x_2, x_3) = (0, 0, 1)$ . For the coefficients  $r(k, m, n)$  Gaussian random variables are chosen. To illustrate the dependence on the numerically chosen cut-off in  $k$ , consider at first a model with  $\Omega_{\text{mat}} = \Omega_{\text{tot}} = 0.3$  as in [32]. In figure 4 the CMB anisotropy is computed using the very low cut-off at  $k_c = 10$ . The coordinate system is chosen such that the horn lies at the equator at one fourth from the left. One observes a suppression of the anisotropy in the horn as discussed above. In figure 5 the cut-off is increased to  $k_c = 140$  and no suppression is observed. The figure 6 represents the anisotropy  $\delta T$  along the equator in the coordinate system of figures 4 and 5 (the horizontal line bisecting the sky map). The horn lies at  $\theta = \frac{\pi}{2}$ . The full curve shows the anisotropy for a cut-off

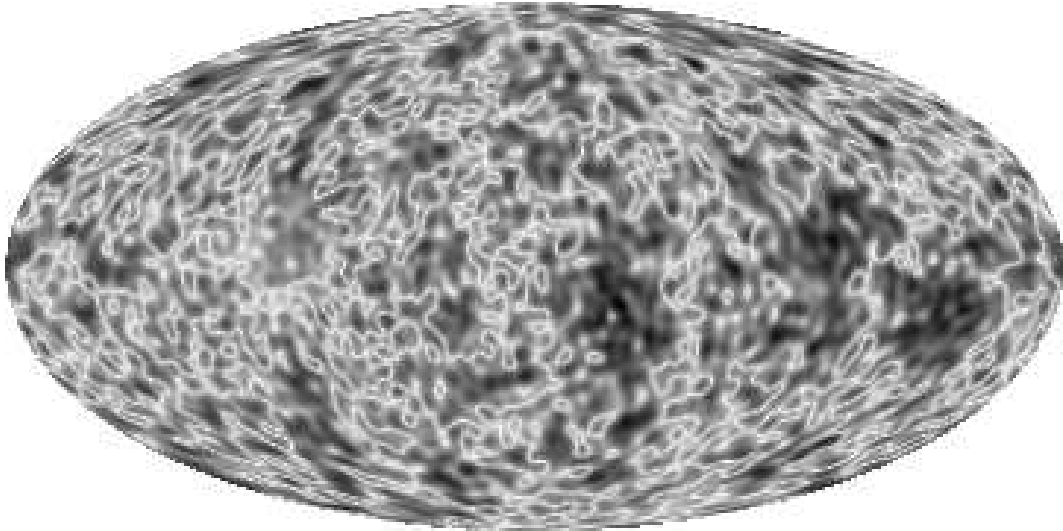


**Figure 5.** The CMB anisotropy  $\delta T$  for the Sokolov-Starobinskii model for  $\Omega_{\text{mat}} = 0.3$  and  $\Omega_{\Lambda} = 0$  with a cut-off  $k_c = 140$  using a Gaussian superposition of the modes (11).

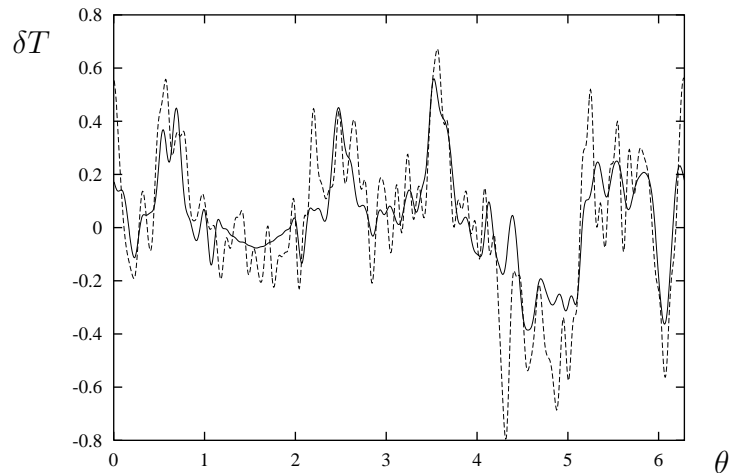


**Figure 6.** The CMB anisotropy  $\delta T$  along the equator of figures 4 and 5. The suppression in the direction of the horn at  $\theta = \frac{\pi}{2}$  is clearly visible in the case of the  $k_c = 10$  cut-off (full curve). In the case of the  $k_c = 140$  cut-off (dashed curve) there are now fluctuations towards the horn.

at  $k_c = 10$  revealing clearly a suppression of the anisotropy around  $\theta = \frac{\pi}{2}$ . The dashed curve presenting the  $k_c = 140$  cut-off displays anisotropies also in the horn.

Up to now we have computed the CMB anisotropy solely with the eigenmodes (11) and have ignored the plane wave solutions (13). These solutions contribute significantly towards the horn. As can be observed from figure 6 there are fluctuations for a sufficiently high chosen cut-off in  $k$ , but these fluctuations are smaller than farther away from the horn. This is due to the current restriction to the eigenmodes (11). The plane wave solutions have significant contributions especially in the direction of the horn as shown in figure 7. We now compute the CMB anisotropy for the model with  $\Omega_{\text{tot}} = 0.3$  and a cut-off  $k_c = 140$  using all three types of modes. We use for the

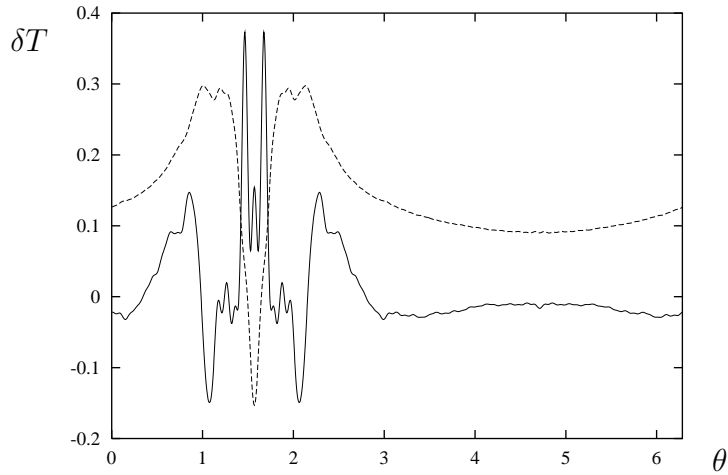


**Figure 7.** The CMB anisotropy  $\delta T$  along the equator of the sine (full curve) and cosine (dashed curve) plane wave solutions (13) using a Gaussian superposition. The contribution from the cosine plane waves is multiplied by a factor of  $-\frac{1}{6}$  in order to get fluctuations comparable to the sine plane wave contribution.

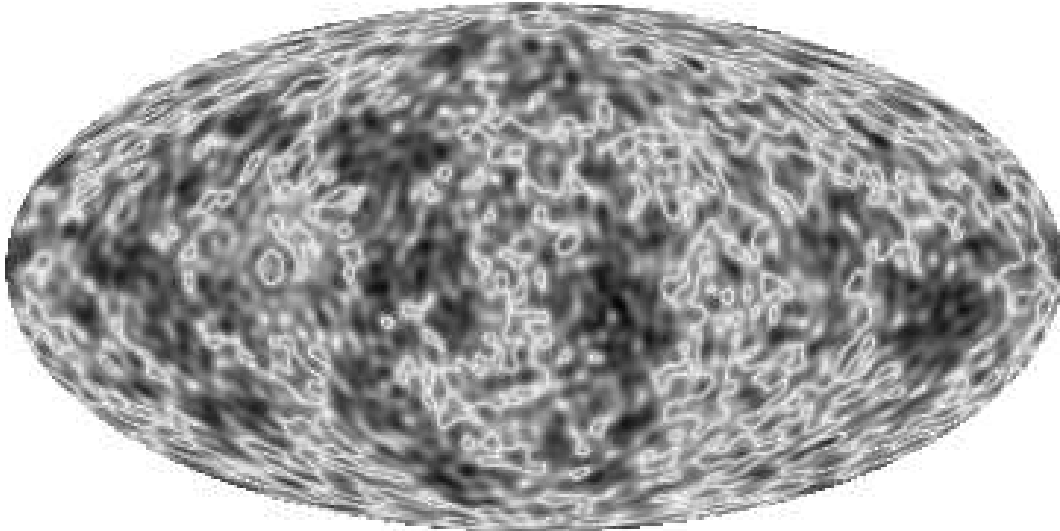


**Figure 8.** The CMB anisotropy  $\delta T$  for the Sokolov-Starobinskii model for  $\Omega_{\text{mat}} = 0.3$  and  $\Omega_{\Lambda} = 0$  with a cut-off  $k_c = 140$ . A Gaussian superposition of all three types of modes is shown, i.e. the modes (11) and the sine and cosine plane waves (13). The contribution from the cosine plane waves is weighted by a factor of  $-\frac{1}{6}$ .

coefficients  $r(k, m, n)$  Gaussian random variables. The result is presented in figure 8 showing the CMB sky map and in figure 9 showing the anisotropy along the equator. As can be seen in figures 8 and 9, taking the sine and cosine plane waves into account increases the amplitude of the fluctuations towards the horn. Thus the fluctuations do not betray the horned topology. Since we use Gaussian random variables as coefficients, there is also no fine tuning in contrast to what is stated in [27].

After having shown that the horn can be masked by the CMB fluctuations, let us now turn to the statistical properties of the CMB anisotropy. Expanding the

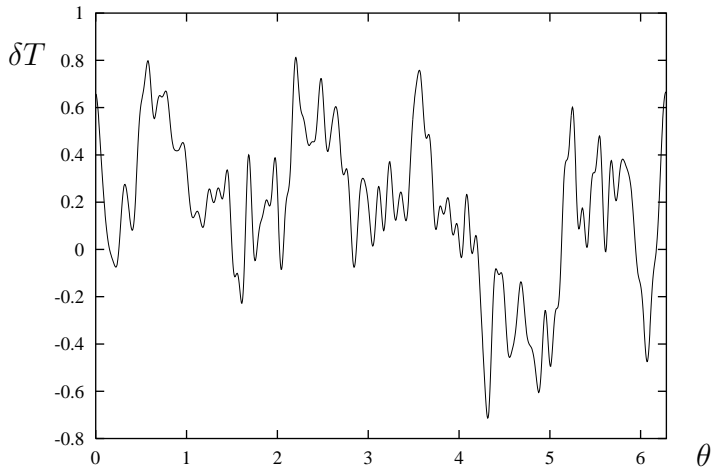


**Figure 9.** The CMB anisotropy is shown at the equator of the sky map from figure 8.

temperature fluctuations with respect to spherical harmonics  $Y_l^m$  yields the expansion coefficients  $a_{lm}$  which in turn lead to the multipoles  $C_l$ , see eq. (1). The angular power spectrum  $\delta T_l^2 = l(l+1)C_l/2\pi$  is shown in figure 10 for the model where the superposition of all modes is used, i. e. for the anisotropy shown in figure 8. Only large angular scales, i. e. multipoles with  $l < 65$ , are shown since higher values of  $l$  would require modes above our numerical cut-off at  $k_c = 140$ . The values of  $\delta T_l^2$  display a flat spectrum up to  $l \simeq 40$  as it is also revealed by the WMAP data [12]. (The error bars of the WMAP data shown in figure 10 do not include the cosmic variance since we compare one-sky realizations.) The large fluctuations of  $\delta T_l^2$  in our model arise from the fact that we compute these values for a fixed observer and not, like CMBFast or CAMB, as a statistical average. The WMAP data display a very low quadrupole moment which is not reproduced by this simulation. This is due to the infinite volume of the Sokolov-Starobinskii fundamental cell. This contrasts to the Picard cell which is discussed in the next section.

Let us now turn to the correlation function  $C(\vartheta)$  which emphasizes the large angular scales and thus the low  $l$ -range. In figure 11  $C(\vartheta)$  is shown (full curve) in comparison with the WMAP data [12] (dashed curve). A large deviation from the WMAP data is revealed near  $\vartheta = 0^\circ$  since our computation takes only the values of  $C_l$  with  $l \leq 65$  into account. The model does not describe the correlation hole for  $\vartheta \gtrsim 160^\circ$  as observed by WMAP which is due to the very small observed quadrupole moment  $C_2$ .

Up to now we have only discussed a model with  $\Omega_{\text{tot}} = 0.3$ . However, current cosmological observations now point to a nearly flat universe. Therefore we show in figure 12 angular power spectra  $\delta T_l^2$  for models with  $\Omega_{\text{tot}} = 0.9$  and  $\Omega_{\text{tot}} = 0.95$ . We use here only the eigenmodes (11) up to  $k_c = 140$  and ignore the plane waves. In order to obtain the correct values for higher values of  $l$  the contribution of modes above  $k = 140$  is taken into account by assuming that their spherical expansion with respect to the observer point yields Gaussian expansion coefficients  $a_{lm}$ , i. e. that they

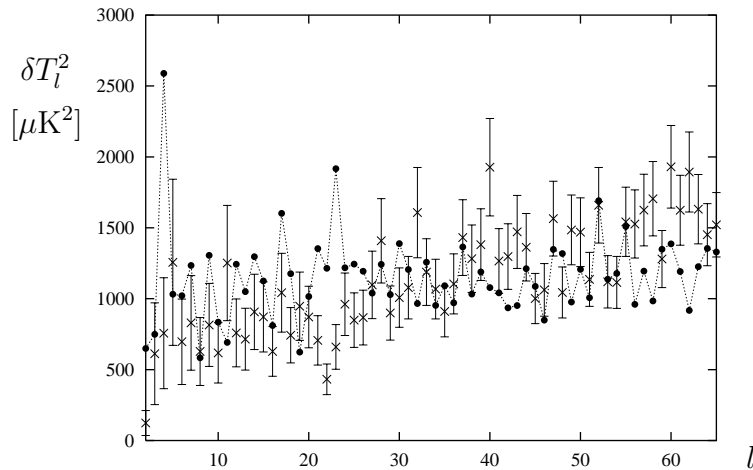


**Figure 10.** The angular power spectrum  $\delta T_l^2 = l(l+1)C_l/2\pi$  is shown for the sky map from figure 8 as dots. The crosses with error bars are the first year WMAP data [12].

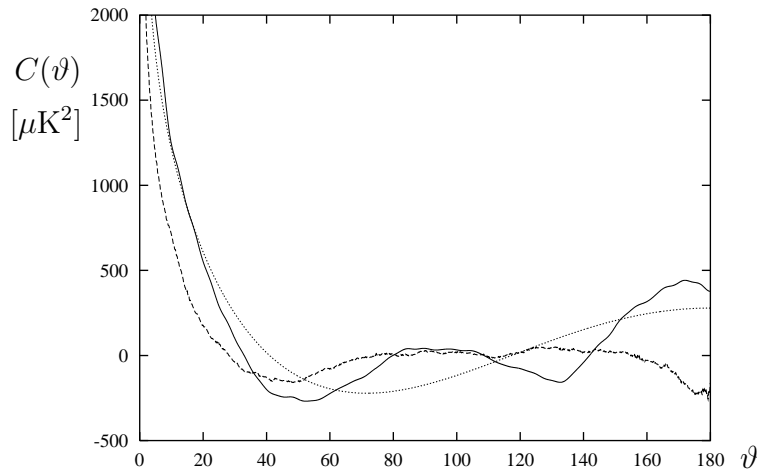


**Figure 11.** The temperature correlation function  $C(\vartheta)$  is shown as a full curve for the sky map from figure 8. The corresponding WMAP curve is displayed as a dashed curve. The dotted curve represents the best  $\Lambda$ CDM model described in [47].

are statistically isotropic. Under this assumption, the  $k$ -integral in (8) is for  $k > 140$  evaluated analogously to the CMBFast method. In figure 12a) we choose  $\Omega_{\text{mat}} = 0.3$ ,  $\Omega_{\Lambda} = 0.6$ , in figure 12b)  $\Omega_{\text{mat}} = 0.3$ ,  $\Omega_{\Lambda} = 0.65$  and in figure 12c)  $\Omega_{\text{mat}} = 0.35$ ,  $\Omega_{\Lambda} = 0.6$ . In all three cases an approximately flat spectrum is observed having up to values of  $l = 65$  fluctuations of the same order as the WMAP data. The topological structure of the Sokolov-Starobinskii model produces no signature in the angular power spectrum. Thus if our Universe would possess a small negative curvature with the Sokolov-Starobinskii topology, the CMB anisotropy would not reveal this “horned” topology.



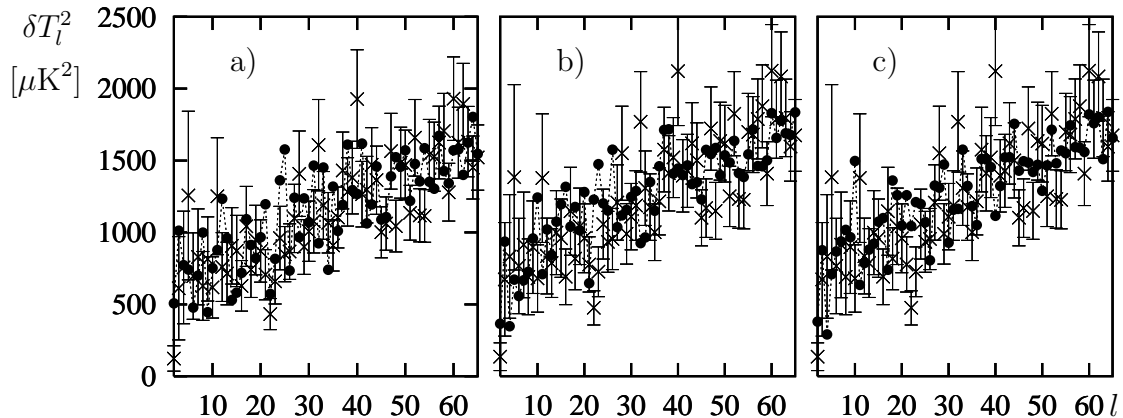


**Figure 12.** The angular power spectrum  $\delta T_l^2 = l(l+1)C_l/2\pi$  is shown (full dots) for three nearly flat Sokolov-Starobinskii models having a)  $\Omega_{\text{mat}} = 0.3$ ,  $\Omega_{\Lambda} = 0.6$ , b)  $\Omega_{\text{mat}} = 0.3$ ,  $\Omega_{\Lambda} = 0.65$  and c)  $\Omega_{\text{mat}} = 0.35$ ,  $\Omega_{\Lambda} = 0.6$ . The cruxes with error bars are the first year WMAP data [12].

#### 4. The Picard model

The crucial difference between the Sokolov-Starobinskii model and the Picard model [28] is that the volume of the Picard model is finite. This is achieved by cutting off the lower ( $x_3 \rightarrow 0$ ) part of the Sokolov-Starobinskii model which leads to the infinite volume. In the Picard model one chooses  $a = 1$  and  $b = 1$  for the periodical identification in the  $x_1$ - and  $x_2$ -directions, respectively. In addition to these two identifications, in the Picard model all points are identified with those which are inverted at the unit sphere having radius 1 and its center at  $\vec{x} = (0, 0, 0)$ . To describe this transformation let us represent the points  $\vec{x} \in \mathfrak{H}_3$  by Hamilton quaternions,  $q = x_1 + ix_2 + jx_3$ , with the multiplication defined by  $i^2 = -1, j^2 = -1, ij + ji = 0$  plus the property that  $i$  and  $j$  commute with every real number. The inverse of a quaternion  $q = q_1 + q_2i + q_3j + q_4ij \neq 0$  is then given by  $q^{-1} = |q|^{-2}(q_1 - q_2i - q_3j - q_4ij)$ , where  $|q|^2 = q_1^2 + q_2^2 + q_3^2 + q_4^2$ . The Picard group  $\Gamma$  is then generated by two translations and one inversion,

$$q \mapsto q + 1, \quad q \mapsto q + i, \quad q \mapsto -q^{-1} \quad . \quad (16)$$

The transformations  $\gamma$  in  $\mathfrak{H}_3$  are given by linear fractional transformations

$$q \mapsto \gamma q = (aq + b)(cq + d)^{-1} \quad ; \quad a, b, c, d \in \mathbb{C} \quad ; \quad ad - bc = 1 \quad .$$

The group of these transformations is up to a common sign isomorphic to the group of matrices of  $\text{PSL}(2, \mathbb{C})$ . The inversion  $q \mapsto -q^{-1}$  bounds the fundamental domain by the unit sphere from below. From the three generating transformations (16) one can compose the transformation  $q \mapsto iq_i$  which corresponds to a rotation by  $180^\circ$  around the  $x_3$ -axis. This rotation together with the inversion  $q \mapsto -q^{-1}$  are the new identifications in comparison with the Sokolov-Starobinskii model. The fundamental

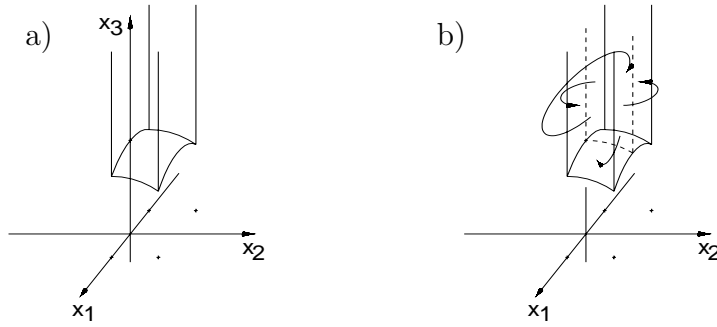


**Figure 13.** The fundamental domain of the Picard group and the identifications of the surfaces.

domain of standard shape is then given by [28, 48]

$$\mathcal{F} = \left\{ q = x_1 + ix_2 + jx_3 \mid -\frac{1}{2} < x_1 < \frac{1}{2}, 0 < x_2 < \frac{1}{2}, |q| > 1 \right\}, \quad (17)$$

see also figure 13. The fundamental domain  $\mathcal{F}$  is a hyperbolic pyramid with one vertex at  $\infty$  and the other four vertices in the points  $P_1 = -\frac{1}{2} + \frac{\sqrt{3}}{2}j$ ,  $P_2 = \frac{1}{2} + \frac{\sqrt{3}}{2}j$ ,  $P_3 = \frac{1}{2} + \frac{1}{2}i + \frac{\sqrt{2}}{2}j$ , and  $P_4 = -\frac{1}{2} + \frac{1}{2}i + \frac{\sqrt{2}}{2}j$ . The volume of this non-compact orbifold  $\Gamma \backslash \mathfrak{H}_3$  is finite [49],

$$\text{vol}(\Gamma \backslash \mathfrak{H}_3) = \frac{\zeta_K(2)}{4\pi^2} = 0.30532186\dots \quad (18)$$

where

$$\zeta_K(s) = \frac{1}{4} \sum_{\nu \in \mathbb{Z}[i] - \{0\}} (\nu\bar{\nu})^{-s}, \quad \Re s > 1,$$

is the Dedekind zeta function, and  $\mathbb{Z}[i] = \mathbb{Z} + i\mathbb{Z}$  are the Gaussian integers.

Due to the additional inversion, the non-trivial eigenfunctions of the Laplace-Beltrami operator are more complicated than in the Sokolov-Starobinskii case and are not known analytically. The eigenfunctions are the so-called Maaß waveforms [50] which are automorphic, i. e. satisfy  $\psi(\gamma q) = \psi(q) \forall \gamma \in \Gamma$ ,  $q \in \mathfrak{H}_3$ , and therefore periodic in  $x_1$  and  $x_2$ . It follows then that they can be expanded into a Fourier series with respect to  $x_1$  and  $x_2$

$$\psi_k(\vec{x}) = u(x_3) + \sum_{(m+in) \in \mathbb{Z}[i] - \{0\}} a_{kmn} x_3 K_{ik}(Qx_3) e^{2\pi i(mx_1 + nx_2)}, \quad (19)$$

where  $Q = 2\pi\sqrt{m^2 + n^2}$  and

$$u(x_3) = \begin{cases} b_0 x_3^{1+ik} + b_1 x_3^{1-ik} & \text{if } k \neq 0 \\ b_2 x_3 + b_3 x_3 \ln x_3 & \text{if } k = 0 \end{cases}. \quad (20)$$

(Here we write  $\psi(\vec{x}) = \psi(x_1, x_2, x_3)$  instead of  $\psi(q)$ .)  $K_{ik}(z)$  denotes again the  $K$ -Bessel function whose order is connected with the eigenvalue  $E$  by  $E = k^2 + 1$ . If a Maaß waveform vanishes in the cusp,

$$\lim_{x_3 \rightarrow \infty} \psi_k^{\text{cusp}}(\vec{x}) = 0, \quad (21)$$

it is called a Maaß cusp form. Maaß cusp forms have  $b_0^{\text{cusp}} = b_1^{\text{cusp}} = b_2^{\text{cusp}} = b_3^{\text{cusp}} = 0$  and are square integrable over the fundamental domain,  $\langle \psi_k^{\text{cusp}}, \psi_k^{\text{cusp}} \rangle < \infty$ , where

$$\langle \psi, \psi' \rangle = \int_{\mathcal{F}} d\mu \psi \psi' \quad \text{with} \quad d\mu = \frac{dx_1 dx_2 dx_3}{x_3^3} . \quad (22)$$

The coefficients  $a_{kmn}^{\text{cusp}}$  in (19) are not free expansion coefficients as in the Sokolov-Starobinskii model, but are uniquely determined for each eigenvalue  $k$ . This is due to the additional symmetry operation of the Picard cell.

According to the Roelcke-Selberg spectral resolution of the Laplacian [51, 52, 53], its spectrum contains both a discrete and a continuous part. The discrete part is spanned by the constant eigenfunction  $\psi_{k_0}^{\text{cusp}} = \text{vol}(\mathcal{F})^{-1/2}$  and a countable number of Maaß cusp forms  $\psi_{k_1}^{\text{cusp}}, \psi_{k_2}^{\text{cusp}}, \psi_{k_3}^{\text{cusp}}, \dots$  which we take to be ordered with increasing eigenvalues,  $0 = E_0 < E_1 \leq E_2 \leq E_3 \leq \dots$ . The smallest nontrivial eigenvalue is  $E_1 = 43.8522464 \dots$  [30]. Recall that the corresponding modes (11) in the Sokolov-Starobinskii model possess a continuous spectrum due to the missing inversion symmetry.

The continuous part of the spectrum  $E \geq 1$  is spanned by the Eisenstein series  $\psi_k^{\text{Eisen}}(\vec{x})$  which are known analytically [54, 55]. Their Fourier coefficients are given by

$$b_0^{\text{Eisen}} = \frac{1}{\sqrt{\pi}} \frac{\Lambda_K(1+ik)}{|\Lambda_K(1+ik)|} , \quad b_1^{\text{Eisen}} = \frac{1}{\sqrt{\pi}} \frac{\Lambda_K(1-ik)}{|\Lambda_K(1+ik)|} , \quad (23)$$

and  $b_2^{\text{Eisen}} = b_3^{\text{Eisen}} = 0$  and

$$a_{kmn}^{\text{Eisen}} = \frac{2}{\sqrt{\pi} |\Lambda_K(1+ik)|} \sum_{\lambda, \mu \in \mathbb{Z}[i], \lambda\mu = m+in} \left| \frac{\lambda}{\mu} \right|^{ik} , \quad (24)$$

where

$$\Lambda_K(s) = 4\pi^{-s} \Gamma(s) \zeta_K(s) \quad (25)$$

has an analytic continuation into the complex plane except for a pole at  $s = 1$ . With these coefficients the Eisenstein series are real and normalized  $\langle \psi_k^{\text{Eisen}}, \psi_{k'}^{\text{Eisen}} \rangle = \delta(k - k')$ . In the case of the Sokolov-Starobinskii model one has  $a_{kmn} = 0$ , and  $b_0$  and  $b_1$  were chosen to obtain the real plane wave solutions (13).

Normalizing the Maaß cusp forms according to  $\langle \psi_k^{\text{cusp}}, \psi_k^{\text{cusp}} \rangle = 1$ , we can expand any square integrable function  $\phi \in L^2(\Gamma \backslash \mathfrak{H}_3)$  in terms of Maaß waveforms, [48],

$$\phi(\vec{x}) = \sum_{n \geq 0} \langle \psi_{k_n}^{\text{cusp}}, \phi \rangle \psi_{k_n}^{\text{cusp}}(\vec{x}) + \int_0^\infty dk \langle \psi_k^{\text{Eisen}}, \phi \rangle \psi_k^{\text{Eisen}}(\vec{x}) . \quad (26)$$

Since the discrete eigenvalues and their associated Maaß cusp forms are not known analytically, one has to compute them numerically. We use the Maaß cusp forms computed along the lines described in [31]. (See [31, 56] for further references concerning the computation of the Maaß wave forms. For earlier computations see [30].)

In figures 14 and 15 we present two CMB simulations having  $\Omega_{\text{tot}} = 0.95$ , the first having  $\Omega_{\text{mat}} = 0.30$  and the second  $\Omega_{\text{mat}} = 0.35$ . Here only the cusp forms up to  $k_c = 140$  are used. The observer is located in the upper half-space at  $\vec{x} = (0.2, 0.1, 1.6)$ . As in the case of the Sokolov-Starobinskii model no suppression of anisotropy is observed towards

the horn which lies at the equator at one fourth from the left, as in the previous sky maps. The figures 16 and 17 show the corresponding angular power spectra  $\delta T_l^2$ . These spectra have a very small quadrupole moment as it is observed by WMAP. The next few moments are also well suppressed. The  $k$ -summation in (8) is carried out for  $k < 140$  using the cusp forms. The contribution of modes with  $k > 140$  is approximated assuming statistical isotropy as in figure 12 using the density of modes as it is given by Weyl's law for the cusp forms [29]. The figures 18 and 19 demonstrate that both models describe the temperature correlation function  $C(\vartheta)$  much better than the concordance model. Both models display a very small correlation at large scales,  $\vartheta \gtrsim 60^\circ$ , as observed

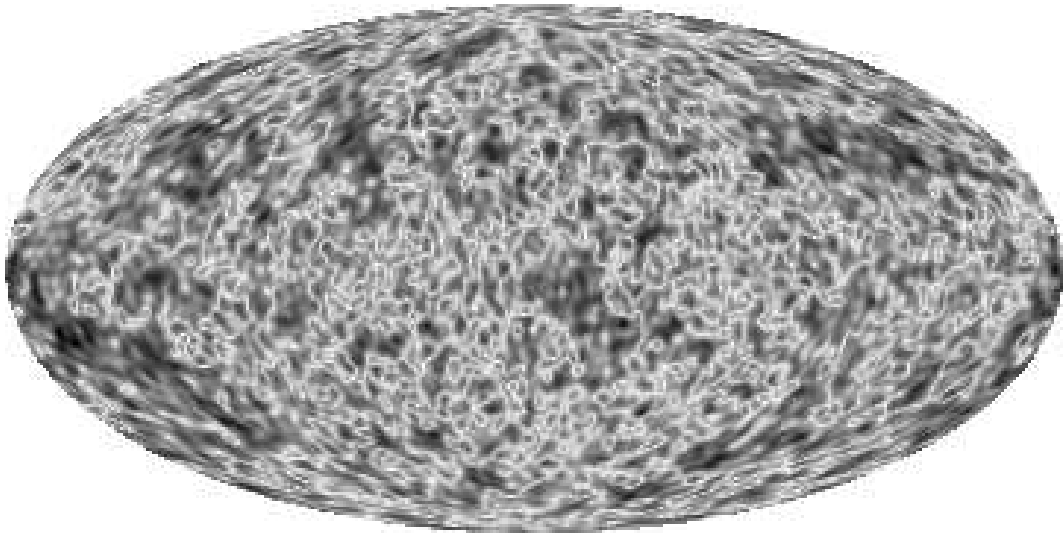


**Figure 14.** The CMB anisotropy  $\delta T$  for the Picard model for  $\Omega_{\text{mat}} = 0.3$  and  $\Omega_\Lambda = 0.65$  with a cut-off  $k_c = 140$  using the cusp forms only. The observer is located in the upper half-space at  $\vec{x} = (0.2, 0.1, 1.6)$ .

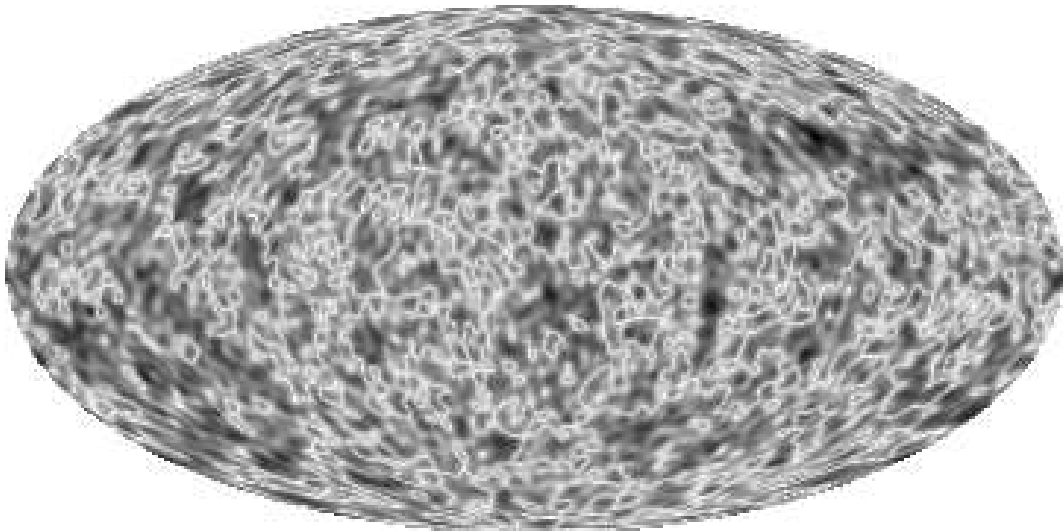


**Figure 15.** The CMB anisotropy  $\delta T$  for the Picard model for  $\Omega_{\text{mat}} = 0.35$  and  $\Omega_\Lambda = 0.60$  with a cut-off  $k_c = 140$  using the cusp forms only. The observer is located in the upper half-space at  $\vec{x} = (0.2, 0.1, 1.6)$ .

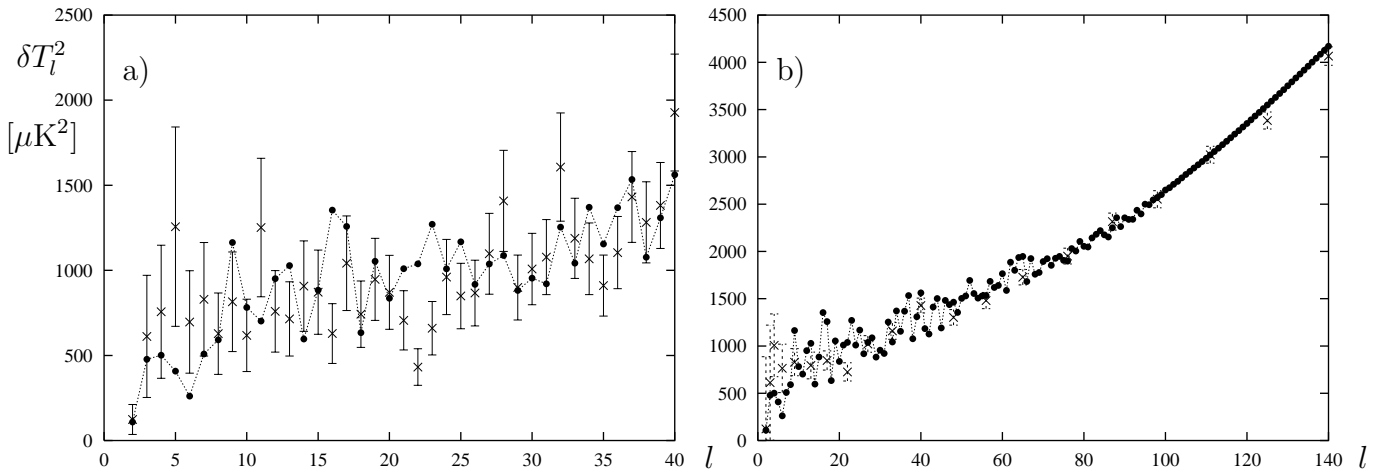


**Figure 16.** The angular power spectrum  $\delta T_l^2 = l(l+1)C_l/2\pi$  is shown as dots for the sky map displayed in figure 14. The crosses with error bars are the first year WMAP data.

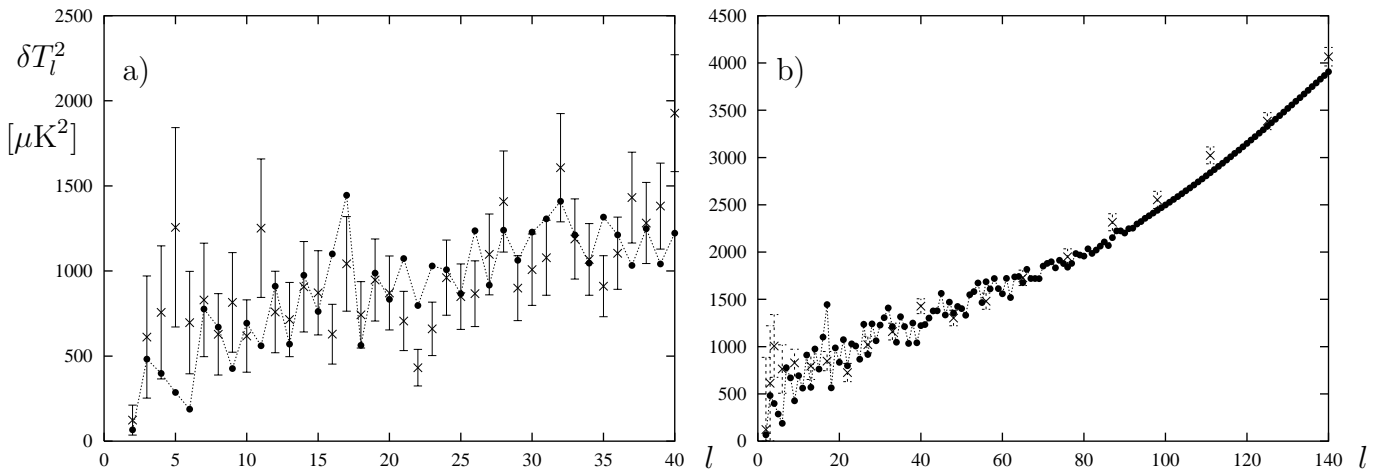


**Figure 17.** The same as in figure 16 but for the sky map displayed in figure 15.

by WMAP. In addition, the two models agree even at smaller scales,  $\vartheta \simeq 10^\circ$ , with the observations much better than the concordance model. This is due to the finite volume of the Picard cell as can be seen in comparison with figure 11 for the Sokolov-Starobinskii cell which has infinite volume. Figure 11 shows that the theoretical curve for the Sokolov-Starobinskii model oscillates around the curve of the concordance model.

In figure 20 the CMB anisotropy  $\delta T$  is shown for an observer who is much higher in the horn at  $\vec{x} = (0.2, 0.1, 5.0)$ . This is indeed very “high” in the horn as can be seen by comparing the volume  $V_\uparrow$  of the fundamental cell (17) “above” the observer in the direction of the horn, i.e. the volume with  $x_3 > x_3^{\text{obs}}$ , with the volume  $V_\downarrow = \text{vol}(\Gamma \backslash \mathfrak{H}_3) - V_\uparrow$  “below”. Due to the hyperbolic volume element  $d\mu$ , the volume above the observer is  $V_\uparrow = \frac{1}{2} \int_{x_3^{\text{obs}}}^\infty dx_3/x_3^3 = \frac{1}{4}(x_3^{\text{obs}})^{-2}$ ,  $x_3^{\text{obs}} > 1$ . In the previous simulations for the Picard model, the observer was located at  $x_3^{\text{obs}} = 1.6$  for which

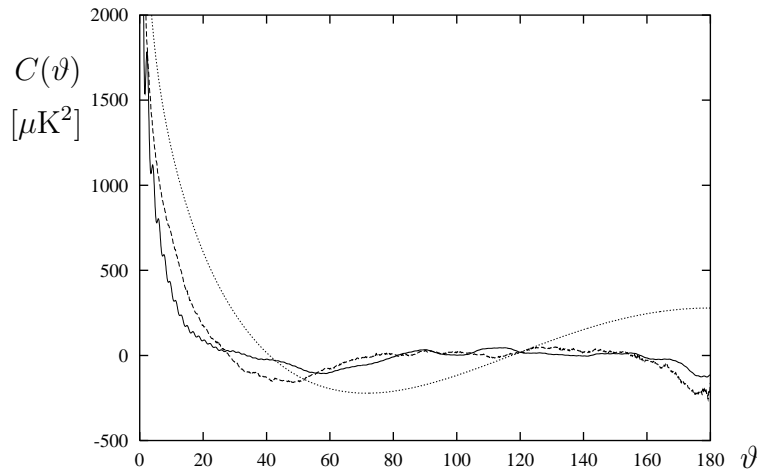


**Figure 18.** The temperature correlation function  $C(\vartheta)$  is shown as a full curve for the sky map displayed in figure 14, i. e. with  $\Omega_{\text{mat}} = 0.3$  and  $\Omega_{\Lambda} = 0.65$ . The corresponding WMAP curve is shown as a dashed curve. The dotted curve represents the best  $\Lambda$ CDM model described in [47].

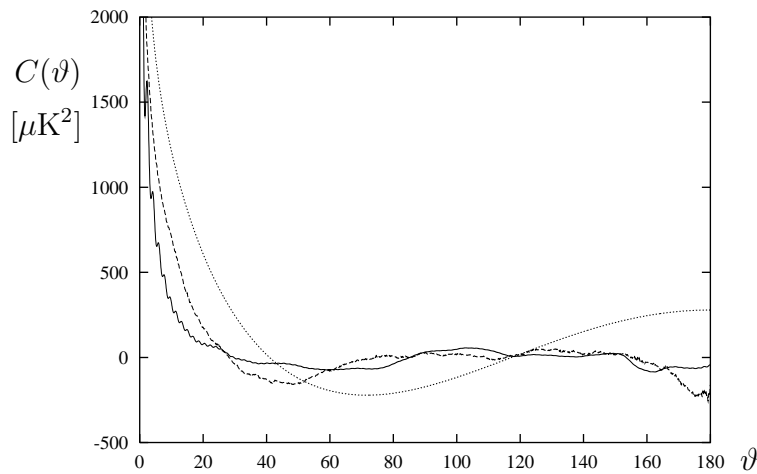


**Figure 19.** The temperature correlation function  $C(\vartheta)$  is shown as a full curve for the sky map displayed in figure 15, i. e. with  $\Omega_{\text{mat}} = 0.35$  and  $\Omega_{\Lambda} = 0.6$ . The corresponding WMAP curve is shown as a dashed curve. The dotted curve represents the best  $\Lambda$ CDM model described in [47].

one obtains  $V_{\downarrow} \simeq 0.207$  and  $V_{\uparrow} \simeq 0.0976$ , i. e. roughly one third of the total volume lies in the direction of the horn. For the observer of figure 20 high in the horn with  $x_3^{\text{obs}} = 5$  one obtains  $V_{\downarrow} \simeq 0.295$  and  $V_{\uparrow} = 0.01$ . Thus this observer point is very improbable but we want to stress here that even such an extreme position does not betray the horn topology in the CMB anisotropy. The figure 21 displays the corresponding temperature correlation function  $C(\vartheta)$ . Again there is very low correlation for  $\vartheta \gtrsim 20^\circ$ . In this case the observed anticorrelation for  $\vartheta \gtrsim 160^\circ$  is not well reproduced. But nevertheless the overall agreement with WMAP data is much better than for the concordance model.

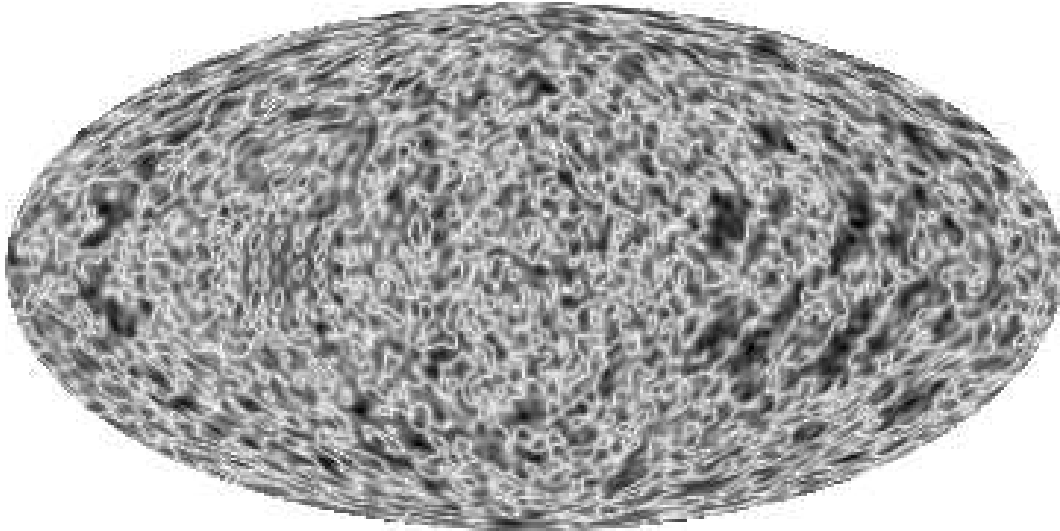


**Figure 20.** The CMB anisotropy  $\delta T$  for the Picard model for  $\Omega_{\text{mat}} = 0.3$  and  $\Omega_{\Lambda} = 0.65$  with a cut-off  $k_c = 140$  using the cusp forms. The observer is located in the upper half-space at  $\vec{x} = (0.2, 0.1, 5.0)$ .

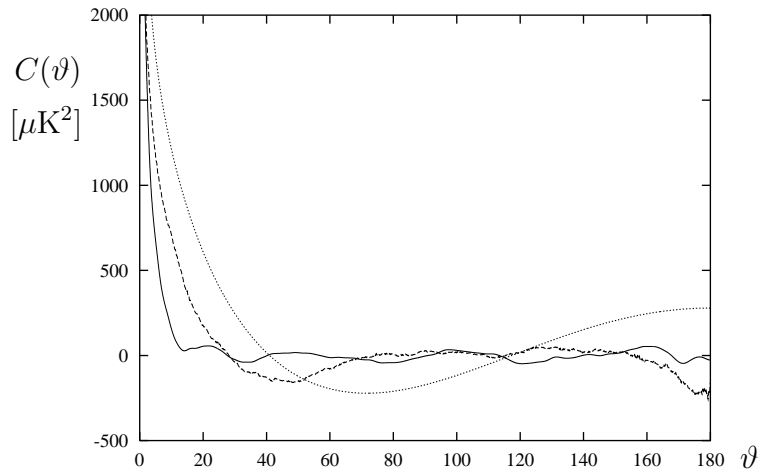


**Figure 21.** The temperature correlation function  $C(\vartheta)$  is shown as a full curve for the sky map displayed in figure 20, i. e. with the observer sitting “high” in the horn and for  $\Omega_{\text{mat}} = 0.30$  and  $\Omega_{\Lambda} = 0.65$ . The corresponding WMAP curve is shown as a dashed curve. The dotted curve represents the best  $\Lambda$ CDM model described in [47].

Now let us consider a superposition of the contributions of the cusp forms and the Eisenstein series. The following model has  $\Omega_{\text{mat}} = 0.3$  and  $\Omega_{\Lambda} = 0.65$ . In figure 22 the CMB anisotropy  $\delta T$  is shown where the Eisenstein series is weighted by a factor  $\alpha = \frac{1}{5}$  relative to the contribution of the cusp forms. This factor depends on the chosen discretization of the  $k$ -integration as discussed above. Using a discretization finer than  $N = 16$ , i. e. 16 evaluation points per unit interval, would allow a larger factor. Since the summation of the cusp forms is not arbitrary, there are values of  $N$  for which this factor can be one. The corresponding temperature correlation function  $C(\vartheta)$  shown in figure 23 displays a very small correlation for  $\vartheta \gtrsim 60^\circ$  and the observed anticorrelation

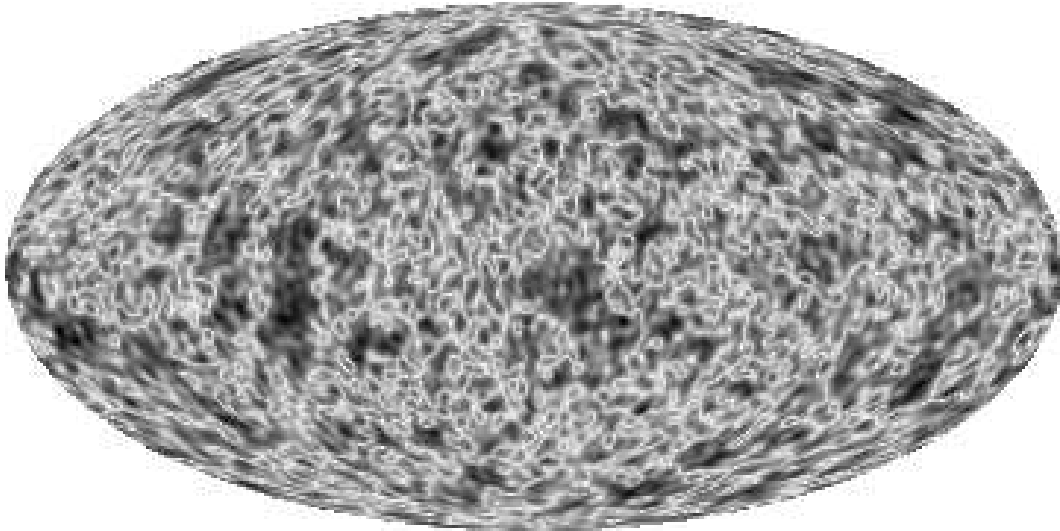


**Figure 22.** The CMB anisotropy  $\delta T$  for the Picard model for  $\Omega_{\text{mat}} = 0.3$  and  $\Omega_{\Lambda} = 0.65$  with a cut-off  $k_c = 140$  for a superposition of cusp forms and Eisenstein series ( $\alpha = \frac{1}{5}$ ). The observer is located in the upper half-space at  $\vec{x} = (0.2, 0.1, 1.6)$ .

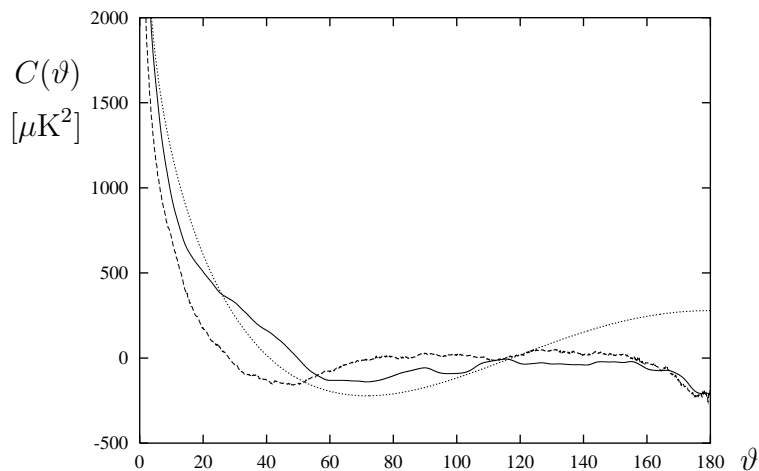


**Figure 23.** The temperature correlation function  $C(\vartheta)$  is shown as a full curve for the sky map displayed in figure 22 using cusp forms as well as the Eisenstein series ( $\Omega_{\text{mat}} = 0.30$  and  $\Omega_{\Lambda} = 0.65$ ). The corresponding WMAP curve is shown as a dashed curve. The dotted curve represents the best  $\Lambda$ CDM model described in [47].

for  $\vartheta \gtrsim 160^\circ$  is matched very well.

## 5. Summary

A large part of this paper was devoted to the question of the existence of flat spots in the CMB sky maps for universes with a horned topology. By the example of two such universes, the Sokolov-Starobinskii model and the Picard model, we showed that the infinitely long horn does not lead to flat spots, i.e. to a suppression of the CMB fluctuations in the horn, if the wavenumber cut-off  $k_c$  is chosen sufficiently large. The



flat spots reported earlier [32, 3] are thus seen as the result of taking not enough modes into account in the expansion of the metric perturbation. We conclude that the CMB sky maps do not reveal a signature of the horned topology in form of flat spots.

Another main point of this paper was to show that a universe with a horned topology, but with a finite volume, such as the Picard model, can explain the loss of power at large angular scales in the CMB anisotropy, as observed by COBE and WMAP. However, if the volume is infinite, as in the Sokolov-Starobinskii model, we have demonstrated that the low quadrupole moment is not reproduced. There is, however, some controversy of how serious one has to take this low value. The small values of the first few multipole moments  $C_l$  have, on the one hand, not been taken so serious to require some new physics, but rather have been considered as a manifestation of cosmic variance or an insufficient consideration of Galactic emission [18] or caused by the local supercluster [57]. From this point of view the Sokolov-Starobinskii model is a viable model. On the other hand, the suppression has been taken as a hint to new physics such as new information on the inflation potentials [58, 59, 60]. However, these potentials have to be fine-tuned such that the arising power spectra are suppressed around the present day cosmological horizon [59]. Such a fine-tuning is not necessary in the case of a non-trivial topology in a universe with negative spatial curvature due to the Mostow rigidity theorem [61, 62]. Thus if the curvature scale is fixed by the densities  $\Omega_x$ , all side-lengths of the fundamental cell  $\mathcal{F}$  are determined, and in turn the comoving wavenumber  $k$  at which the spectrum is suppressed, not because of the initial power spectrum but simply because of the absence of modes below the lowest wavenumber  $k_1$ .

In models with a non-trivial topology, certain points at the surface of last scattering can be identical due to the periodicity condition. These matching points are located on pairs of circles with the same radius. Along two such circles the temperature fluctuations  $\delta T$  produced by the naive Sachs-Wolfe effect are the same, which is called the circles-in-the-sky signature [63]. In [64] a search for such circles in the WMAP data was carried out for nearly back-to-back circles, i. e. for circles whose centers have a distance greater than  $170^\circ$  and whose radii are greater than  $25^\circ$  on the sky. They found no signature and rule out all topologies having such circles. However, it should be kept in mind that only the naive Sachs-Wolfe contribution leads to identical temperature fluctuations. The integrated Sachs-Wolfe contribution arises on the photon path to the observer, which is not identified for the observer and the “copy” of the observer. The same is valid for the Doppler contribution, since the observer and its copy see another projection of the velocity, in general. Furthermore, there are a lot of other secondary contributions to the temperature fluctuations. Nevertheless, it is claimed in [64] that the naive Sachs-Wolfe contribution is strong enough for the identification of circles-in-the-sky. The Picard model is not ruled out by this work, since there are no nearly back-to-back circles. For the model with  $\Omega_{\text{mat}} = 0.3$  and  $\Omega_\Lambda = 0.65$  with  $x_3 = 1.6$ , we obtain 40 pairs, where the largest distance of the centers is at  $145^\circ$  which is not covered by the study in [64]. The model with  $\Omega_{\text{mat}} = 0.35$  and  $\Omega_\Lambda = 0.6$  has only 32 circle pairs. The number of paired circles increases if the observer is posited higher up in the horn, i. e. at larger values of

$x_3$ . For the extreme position at  $x_3 = 5$  one obtains 275 circle pairs with distances up to  $168.6^\circ$  for  $\Omega_{\text{mat}} = 0.3$  and  $\Omega_\Lambda = 0.65$ . These circles could have been detected in [64]. However, for more generic observers, which are not sitting extremely high in the horn, the separation of the circles is too small such that the model cannot yet be ruled out.

In conclusion, we would like to emphasize again that the Picard model studied in this paper is in nice agreement with the observed suppression of power on large scales in the angular power spectrum of the CMB (see figures 18, 19, 21 and 23). This is in contrast to the concordance model which does not reproduce the experimentally observed suppression at  $\vartheta \gtrsim 60^\circ$  and the observed correlation hole at  $\vartheta \gtrsim 160^\circ$ . If future observations will confirm the WMAP data but with smaller errors, this can be interpreted as a clear hint to a non-trivial topology of our Universe having negative spatial curvature and a finite volume.

## Acknowledgment

Financial support by the Deutsche Forschungsgemeinschaft (DFG) under contract No Ste 241/16-1 and the EC Research Training Network HPRN-CT-2000-00103 is gratefully acknowledged.

## References

- [1] G. F. Smoot *et al.*, *Astrophys. J. Lett.* **396**, L1 (1992).
- [2] M. Lachièze-Rey and J. Luminet, *Physics Report* **254**, 135 (1995).
- [3] J. Levin, *Physics Report* **365**, 251 (2002).
- [4] J. R. Bond, D. Pogosyan, and T. Souradeep, *Class. Quantum Grav.* **15**, 2671 (1998).
- [5] J. R. Bond, D. Pogosyan, and T. Souradeep, *Phys. Rev. D* **62**, 043005 (2000), astro-ph/9912124.
- [6] J. R. Bond, D. Pogosyan, and T. Souradeep, *Phys. Rev. D* **62**, 043006 (2000), astro-ph/9912144.
- [7] N. J. Cornish, D. Spergel, and G. Starkman, *Phys. Rev. D* **57**, 5982 (1998).
- [8] R. Aurich, *Astrophys. J.* **524**, 497 (1999).
- [9] N. J. Cornish and D. Spergel, *Phys. Rev. D* **62**, 087304 (2000), astro-ph/9906401.
- [10] K. T. Inoue, K. Tomita, and N. Sugiyama, *Mon. Not. R. Astron. Soc.* **314**, L21 (2000), astro-ph/9906304.
- [11] R. Aurich and F. Steiner, *Mon. Not. R. Astron. Soc.* **323**, 1016 (2001), astro-ph/0007264.
- [12] G. Hinshaw *et al.*, *Astrophys. J. Supp.* **148**, 135 (2003), astro-ph/0302217.
- [13] C. L. Bennett *et al.*, *Astrophys. J. Supp.* **148**, 97 (2003).
- [14] M. Tegmark, A. de Oliveira-Costa, and A. J. S. Hamilton, *Phys. Rev. D* **68**, 123523 (2003), astro-ph/0302496.
- [15] H. K. Eriksen, A. J. Banday, K. M. Górski, and P. B. Lilje, *Astrophys. J.* **612**, 633 (2004), astro-ph/0403098.
- [16] D. J. Schwarz, G. D. Starkman, D. Huterer, and C. J. Copi, astro-ph/0403353 (2004).
- [17] A. Slosar, U. Seljak, and A. Makarov, *Phys. Rev. D* **69**, 123003 (2004), astro-ph/0403073.
- [18] G. Efstathiou, *Mon. Not. R. Astron. Soc.* **346**, L26 (2003), astro-ph/0306431.
- [19] C. Skordis and J. Silk, astro-ph/0402474 (2004).
- [20] M. Kamionkowski and A. Loeb, *Phys. Rev. D* **56**, 4511 (1997).
- [21] S. Y. Sazonov and R. A. Sunyaev, *Mon. Not. R. Astron. Soc.* **310**, 765 (1999).
- [22] N. Seto and M. Sasaki, *Phys. Rev. D* **62**, 123004 (2000).
- [23] S. Chandrasekhar, *Mitteilungen der Astron. Gesellschaft Hamburg* **67**, 19 (1986).

- [24] K. Schwarzschild, *Gesammelte Werke / Collected Works, Vol. 1* (Springer, Berlin, 1992), edited by H. H. Voigt.
- [25] K. Schwarzschild, *Vierteljahrsschrift der Astron. Gesellschaft* **35**, 337 (1900).
- [26] K. Schwarzschild, *Class. Quantum Grav.* **15**, 2539 (1998), translated by J. M. Stewart.
- [27] D. D. Sokolov and A. A. Starobinskii, *Sov. Astron.* **19**, 629 (1976).
- [28] E. Picard, *Bull. Soc. Math. France* **12**, 43 (1884).
- [29] C. Matthies, *Picards Billard: Ein Modell für Arithmetisches Quantenchaos in drei Dimensionen*, PhD thesis, Universität Hamburg, II. Institut für Theoretische Physik, 1995.
- [30] G. Steil, Eigenvalues of the Laplacian for Bianchi groups, in *Emerging Applications of Number Theory*, edited by D. A. Hejhal, J. Friedman, M. C. Gutzwiller, and A. M. Odlyzko, IMA Series No. 109, pp. 617–641, Springer, 1999.
- [31] H. Then, Arithmetic quantum chaos of Maaß waveforms, in *Number Theory, Physics, and Geometry*, edited by B. Julia, P. Moussa, P. Cartier, and P. Vanhove, Springer, 2003, math-ph/0305048.
- [32] J. Levin, J. D. Barrow, E. F. Bunn, and J. Silk, *Phys. Rev. Lett.* **79**, 974 (1997).
- [33] R. Aurich and F. Steiner, *Phys. Rev. D* **67**, 123511 (2003), astro-ph/0212471.
- [34] R. Aurich and F. Steiner, *International Journal of Modern Physics D* **13**, 123 (2004), astro-ph/0302264.
- [35] L. Conversi, A. Melchiorri, L. Mersini, and J. Silk, *Astropart. Phys.* **21**, 443 (2004), astro-ph/0402529.
- [36] W. Hu, *Astrophys. J.* **506**, 485 (1998).
- [37] V. G. Gurzadyan *et al.*, *International Journal of Modern Physics D* **12**, 1859 (2003), astro-ph/0210021.
- [38] V. G. Gurzadyan *et al.*, astro-ph/0312305 (2003).
- [39] V. G. Gurzadyan *et al.*, *Nuovo Cim.* **118B**, 1101 (2003), astro-ph/0402399.
- [40] J. Luminet, J. R. Weeks, A. Riazuelo, R. Lehoucq, and J. Uzan, *Nature* **425**, 593 (2003).
- [41] V. F. Mukhanov, H. A. Feldman, and R. H. Brandenberger, *Physics Report* **215**, 203 (1992).
- [42] R. K. Sachs and A. M. Wolfe, *Astrophys. J.* **147**, 73 (1967).
- [43] V. F. Mukhanov, astro-ph/0303072 (2003).
- [44] D. N. Spergel *et al.*, *Astrophys. J. Supp.* **148**, 175 (2003), astro-ph/0302209.
- [45] S. L. Bridle, A. M. Lewis, J. Weller, and G. Efstathiou, *Mon. Not. R. Astron. Soc.* **342**, L72 (2003), astro-ph/0302306.
- [46] J. G. Ratcliffe, *Foundations of Hyperbolic Manifolds* Graduate Texts in Mathematics 149 (Springer, Berlin, 1994).
- [47] C. L. Bennett *et al.*, *Astrophys. J. Supp.* **148**, 1 (2003), astro-ph/0302207.
- [48] J. Elstrodt, F. Grunewald, and J. Mennicke, *Groups Acting on Hyperbolic Space* (Springer, Berlin, 1998).
- [49] G. Humbert, *C. R. Acad. Sci. Paris* **169**, 448 (1919).
- [50] H. Maaß, *Abh. Math. Semin. Univ. Hamburg* **16**, 72 (1949).
- [51] A. Selberg, *J. Indian Math. Soc. (N.S.)* **20**, 47 (1956).
- [52] W. Roelcke, *Math. Ann.* **167**, 292 (1966).
- [53] W. Roelcke, *Math. Ann.* **168**, 261 (1967).
- [54] T. Kubota, *Elementary Theory of Eisenstein Series* (Kodansha, Tokyo and Halsted Press, 1973).
- [55] J. Elstrodt, F. Grunewald, and J. Mennicke, *J. Reine Angew. Math.* **360**, 160 (1985).
- [56] D. A. Hejhal, On eigenfunctions of the Laplacian for Hecke triangle groups, in *Emerging Applications of Number Theory*, edited by D. A. Hejhal, J. Friedman, M. C. Gutzwiller, and A. M. Odlyzko, IMA Series No. 109, pp. 291–315, Springer, 1999.
- [57] L. R. Abramo and L. Sodre Jr, astro-ph/0312124 (2003).
- [58] J. M. Cline, P. Crotty, and J. Lesgourgues, *Journal of Cosmology and Astroparticle Physics* **9**, 10 (2003).
- [59] C. R. Contaldi, M. Peloso, L. Kofman, and A. Linde, *Journal of Cosmology and Astroparticle*

- Physics **7**, 2 (2003).
- [60] B. Feng and X. Zhang, *Physics Letters B* **570**, 145 (2003).
  - [61] G. D. Mostow, *Strong rigidity of locally symmetric spaces* *Annals of Mathematics Studies* No. **78** (Princeton University Press, Princeton, 1973).
  - [62] G. Prasad, *Invent. Math.* **21**, 255 (1973).
  - [63] N. J. Cornish, D. N. Spergel, and G. D. Starkman, *Class. Quantum Grav.* **15**, 2657 (1998).
  - [64] N. J. Cornish, D. N. Spergel, G. D. Starkman, and E. Komatsu, *Phys. Rev. Lett.* **92**, 201302 (2004), astro-ph/0310233.